Numerical simulation of bubble dispersion in turbulent Taylor-Couette flow

A.Chouippe,[1,2,a] E.Climent,[3,4,b] D.Legendre,[3,4] and C.Gabillet[5]
[1] *University of Toulouse, INPT-UPS, Institut de Mécanique des Fluides de Toulouse, 31400, Toulouse -France*
[2] *CNRS, IMFT, Institut de Mécanique des Fluides de Toulouse, 31400 Toulouse - France*
[3] *University of Toulouse, INPT-UPS, Institut de Mécanique des Fluides de Toulouse, France*
[4] *CNRS, IMFT, Institut de Mécanique des Fluides de Toulouse, France*
[5] *IRENav, Institut de Recherche de l' École Navale - Lanvéoc Poulmic, Brest, France*

(Dated: 9 March 2014)

We investigate bubble dispersion in turbulent Taylor-Couette flow. The aim of this study is to describe the main mechanisms yielding preferential bubble accumulation in near-wall structures of the flow. We first proceed to direct numerical simulation of Taylor-Couette flows for three different geometrical configurations (three radius ratios $\eta = R_1/R_2$: $\eta = 0.5$, $\eta = 0.72$ and $\eta = 0.91$ with the outer cylinder at rest) and Reynolds numbers corresponding to turbulent regime ranging from 3000 to 8000. The statistics of the flow are discussed using two different averaging procedures that permit to characterize the mean azimuthal velocity, the Taylor vortices contribution and the small-scale turbulent fluctuations. The simulations are compared and validated with experimental and numerical data from literature. The second part of this study is devoted to bubble dispersion. Bubble accumulation is analyzed by comparing the dispersion obtained with the full turbulent flow field to bubble dispersion occurring at lower Reynolds numbers in previous works. Several patterns of preferential accumulation of bubbles have been observed depending on bubble size and the effect of gravity. For the smaller size considered, bubbles disperse homogeneously throughout the gap, while for the larger size they accumulate along the inner wall for the large gap width ($\eta = 0.5$). Varying the intensity of buoyancy yields complex evolution of the bubble spatial distribution. For low gravity effect, bubble entrapment is strong leading to accumulation along the inner wall in outflow regions (streaks of low wall shear stress). When buoyancy effect dominates on vortex trapping, bubbles rise through the vortices while spiral patterns stretched along the inner cylinder are clearly identified. Force balance is analyzed to identify dominating forces leading to this accumulation and accumulation patterns are compared with previous experiments.

PACS numbers: 47.55.dd ; 47.27.E- ; 47.27.nb
Keywords: Bubbles, Taylor-Couette, turbulence, Numerical simulation, Lagrangian tracking

I. INTRODUCTION

The flow between two rotating concentric cylinders has many industrial applications due to its simple conception and the well controlled shear stress. Applications of multiphase flows in such device are for example liquid-liquid extraction, biological or chemical reactors.

[a] Present address: Institute for Hydromechanics, Karlsruhe Institute of Technology (KIT), Karlsruhe, Germany
[b] Electronic mail: eric.climent@imft.fr

It is also an academic configuration to investigate the effect of successive flow instabilities on the dispersion of bubbles or particles. The aim of our study is to use numerical simulation to evidence major mechanisms leading to bubble accumulation in the Taylor-Couette turbulent regime. The geometry of the Taylor-Couette device is characterized by two dimensionless parameters: the radius ratio $\eta = R_1/R_2$, and the aspect ratio $\Gamma = L_{ax}/(R_2 - R_1)$ where R_1, R_2 and L_{ax} are the inner cylinder radius, outer cylinder radius and height of the cylinders, respectively (see fig. 1). When the outer cylinder is fixed, the Reynolds number

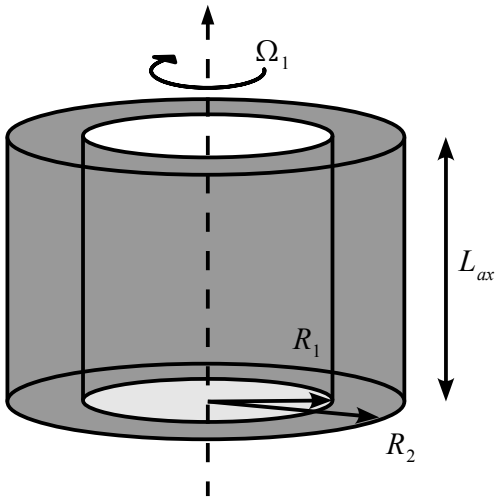

FIG. 1. Geometric configuration of the Taylor-Couette device

characterizing the flow dynamics is based on the velocity of the inner cylinder $U_1 = R_1\Omega_1$, the gap width, and the kinematic viscosity of the fluid ν:

$$Re = \frac{U_1(R_2 - R_1)}{\nu} \tag{1}$$

Taylor-Couette flow experiences successive hydrodynamic instabilities for increasing Re. For low Reynolds numbers the flow is purely azimuthal, and can be solved analytically, e.g. Couette flow. For increasing Reynolds numbers different regimes appear : the first one is the Taylor Vortex Flow regime (TVF), characterized by toroidal steady counter-rotating vortices with an axial periodicity[1]. Then the Wavy Vortex Flow (WVF), Modulated Wavy Vortex Flow (MWVF), Turbulent Taylor Vortex Flow (TTVF), and chaotic Turbulent Flow occur successively at higher Reynolds numbers[2]. The transition to turbulence has been studied[3], with a specific emphasis on the evolution of energy spectra. The fully turbulent regime was also investigated[4]. In our study, we focus on the TTVF regime, which is characterized by the superposition of three distinct contributions as previously discussed[5,6]: the azimuthal flow driven by the rotation of the inner cylinder, large scale Taylor Vortices and small scale turbulent fluctuations. The presence of Taylor Vortices induces the development of two jets (outflow and inflow), respectively directed towards the outer and the inner cylinders. The other specificity of turbulent Taylor-Couette flows is its near-wall turbulence structure composed of small-scale herringbone-like streaks observed experimentally[7] and numerically[8].

The turbulent Taylor-Couette flow is an interesting configuration to study bubble dispersion, since it is made of distinct structures (large and small scale structures). The interaction between bubbles and large scale vortices has already been investigated[9–11]. Studies of the interaction between bubbles and a turbulent flow has been carried out in homogeneous

isotropic turbulence[12] and in turbulent channel flow[13]. It appears that bubbles accumulate in low-pressure and high vorticity regions of the flow.

To our knowledge, four research groups have been very active to study experimentally bubble dispersion in Taylor-Couette configuration: Research Institute of French Naval Academy[14–16], University of Maryland[17,18], the Hokkaido University[19,20], and the University of Twente[21,22]. Table I gives the geometric characteristics of this different devices, and the ranges of Reynolds number which have been considered in the corresponding experiments.

Device	η	Γ	Re
Research Institute of French Naval Academy[14,15]	0.85	$20-22$	$0 \rightarrow 4000$
Research Institute of French Naval Academy[16]	0.9	40	$2500 \rightarrow 3.10^4$
Hokkaido University[19,20]	0.83	20	$600 \rightarrow 4500$
University of Maryland[17]	0.72	11.5	$2.10^5 \rightarrow 10^6$
University of Twente[18,21]	0.716	11.68	$2.10^5 \rightarrow 2.10^6$

TABLE I. Geometric parameters of some bubbly Taylor-Couette devices.

Early studies at IRENav were concerned with TVF, WVF, MWVF and weakly turbulent regimes for gaseous cavitation and ventilation. First measurements were used to quantify the influence of bubbles on the velocity field, and the accumulation patterns of the dispersed phase for different bubble sizes[15]. They observed axial deformation of Taylor vortices and an advance of the transition to MWVF. Bubbles were trapped by the large scale vortices for WVF while they were accumulating near the inner cylinder in outflow regions for MWVF. They observed that sub-millimetric bubbles are rather localized in the outflow region, while millimetric bubbles are trapped within the Taylor vortices (measurements of bubble concentration[16] support those observations). Accumulation in Taylor vortices leads to vorticity enhancement and a reduction of the axial wavelength. Accumulation near the inner cylinder wall increases near-wall velocity gradients in the outflow region.

Other studies had the objective to show if significant modifications of the flow can be achieved by bubble injection (namely, bubble drag reduction). Indeed drag reduction occurs in the MWVF and weakly turbulent regimes[19]. Bubbly drag reduction was also investigated experimentally for higher Reynolds numbers at University of Maryland[17,18] and in the Twente Turbulent Taylor-Couette (T^3C) system[18,21,22]. The T^3C device enables to consider range of Reynolds numbers from 5.10^5 to 2.10^6, and two different drag reduction regimes have been observed: moderate drag reduction for the lower Reynolds numbers and significant drag reduction for the largest. Void fraction measurements in the T^3C highlighted preferential accumulation of bubbles near the inner cylinder. It appeared also that bubble deformability was crucial for viscous drag reduction at very high Reynolds numbers[18,22].

Numerical simulation was used for the study of bubble dispersion in order to analyze migration mechanisms in the TVF and WVF regimes[23] and also for considering bubble drag reduction[24] with results qualitatively consistent with the experiments of Murai et al.[19]. Major results can be summarized as follows. Depending on the size of the bubbles, the rotation rate of the inner cylinder and the intensity of Taylor vortices, bubbles can either accumulate along the inner wall, be trapped in the vortices or in outflow regions. When wavy motion sets in, bubble initially accumulated as collars in toroidal vortices follow the azimuthal deformation of vortices and migrate towards the crests or throughs of the wave. When two-way coupling is enabled[24], bubbles modify the vortex structure and may induce drag reduction due to upward flow perturbation. The aim of our study is to focus on passive bubble dispersion in the Taylor-Couette flows, and more specifically on the turbulent regime (Re ranging from 3000 to 8000), and analyze migration mechanisms by considering three geometric configurations $\eta = 0.5 - 0.72 - 0.91$.

The paper is organized as follows: in the first section we present the numerical method which has been used and validations with experiments or former simulations from the literature. In the second section, we detail the single-phase flow statistics and its spatial structure

(large scale vortices and near-wall turbulent structures). The third part is concerned with bubble dispersion for different bubble size. Then, we propose a discussion on migration mechanisms that contribute to the dispersion.

II. DESCRIPTION OF THE CARRIER FLOW

In this section, we detail the simulation of the turbulent Taylor-Couette flows for single-phase configuration. The final objective is to perform a Direct Numerical Simulation (DNS) of the fluid coupled to Lagrangian tracking of the bubbles. We will first describe the numerical method, and then emphasize the major features characterizing the flow dynamics.

A. Numerical method and validations

The Taylor-Couette flow dynamics is computed by solving the full three-dimensional unsteady Navier-Stokes equations (equations 2,3) for a Newtonian fluid with constant physical properties. The equations are written in the conservative form. The code JADIM is based on a finite volume method, and the velocity and pressure ($\mathbf{U}$,P) are discretized on a staggered nonuniform cylindrical grid. The numerical code has been already used in laminar and turbulent configurations[23,25,26]. The spatial derivatives are computed with second order accuracy, and temporal integration is achieved by a third order Runge-Kutta scheme and a semi-implicit Crank-Nicolson scheme for the viscous terms. Incompressibility is achieved by a projection method associated to a Poisson equation for the pressure correction. Time step is defined in order to have CFL lower than 1.

$$\nabla \cdot \mathbf{u} = 0 \tag{2}$$

$$\frac{\partial \mathbf{u}}{\partial t} + \nabla \cdot (\mathbf{u}\mathbf{u}) = -\frac{1}{\rho}\nabla P + \nabla \cdot \left(\nu \left[\nabla \mathbf{u} + (\nabla \mathbf{u})^T\right]\right) + \mathbf{g} \tag{3}$$

Validations for different Taylor-Couette configurations have been carried out. We impose a constant velocity U_1 on the inner cylinder, and use periodic boundary conditions in the axial direction (so that the configuration is equivalent to infinite cylinders in the axial direction with a prescribed wavelength). Velocities are scaled with U_1, distances with the radius of the outer cylinder R_2. The reference time $T_{\Omega_1} = 2\pi R_1/U_1$ (one revolution of the inner cylinder) has been chosen to describe unsteady features. Imposing periodic boundary conditions sets the number of Taylor vortices in the simulation domain, and then the wavelength λ has to be chosen properly. Linear stability analysis predicts that λ should be close to $2(R_2 - R_1)$ but different ratios $\lambda/(R_2 - R_1)$ could be obtained by changing the acceleration rate during the transient regime[27,28]. History effects (increasing or decreasing Re) could have an influence on the selected wavelength of the flow[29]. We collected values of this ratio from different experimental studies in the literature (see figure 2). It appears that geometries with small gaps (η close to one) are more sensitive to the Reynolds number. From the figure, $\lambda \approx 2(R_2 - R_1)$ seems to be a good estimate for large gap geometries for the range of Re considered in our study. The axial length we selected for our DNS are also reported in this figure.

A good compromise need to be determined between grid refinement for ensuring the DNS of the turbulent flow and the computational time necessarily to reach good convergence of the statistics. For this purpose, we focused on the large gap case ($\eta = 0.5$) for $Re = 8000$ in order to have a direct comparison with the DNS of Dong[5]. The characteristics of the three grids tested are summarized in table II. We fixed $\lambda/(R_2 - R_1) = 2.09$ to match precisely Dong's study (which is a common value for large gap geometry according to figure 2).

We first compared the radial profile of the mean velocity $< \mathbf{U} >_{x\theta t}$ (averaged in time and over the axial and azimuthal directions) with the corresponding simulation[5]. The axial and radial components are close to zero, and the azimuthal component is not very sensitive to the

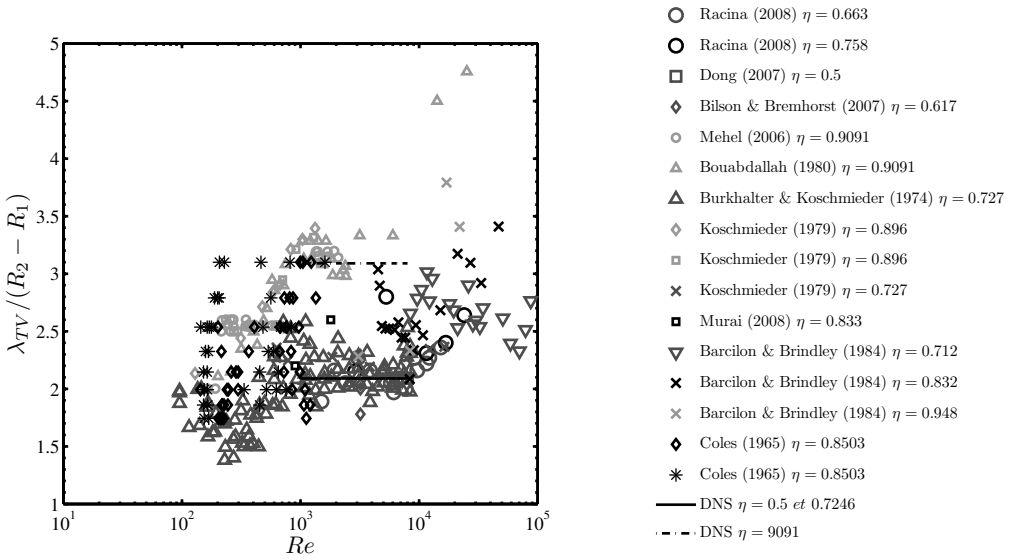

FIG. 2. Axial wavelength of Taylor vortices as a function of the Reynolds number (data gathered from literature[5,6,19,28–34]). Colors are related to three distinct ranges of gap width: grey for $0.5 < \eta < 0.75$, black for $0.75 < \eta < 0.85$ and light grey for $0.85 \leq \eta$.

spatial discretisation as shown in fig. 3.a which is consistent with a similar observation on the torque. The evolution of the fluctuating velocity field defined as $U_i^{'} = U_i - < U_i >_{x\theta t}$ is shown in fig. 3.b for the azimuthal velocity. This quantity is more sensitive to grid refinement, specially when considering the peak values close to the inner and outer walls. Fluctuation levels are larger with coarse grids due to inaccurate calculation at small scales of the dissipation, and we observe the convergence with a good agreement to the Dong's DNS for the finest mesh (which will be selected for the rest of our computations). For the other configurations, we based our criteria of mesh independence on the fluctuation statistics. We chose to simulate one single wavelength in the axial direction and set at least four points in the radial direction within the viscous sublayer $r^+ \leq 5$. Table III summarizes the characteristics of the meshes used in the rest of our study. For the small gap geometry ($\eta = 0.91$), we chose an axial wavelength $\lambda \approx 3.1(R_2 - R_1)$, which is close to the prediction of the linear stability analysis[1] and also in agreement with experimental observations[16].

Mesh name	L_{ax}	N_x	N_r	N_θ	$\Delta x/\lambda$	$\Delta r_1/R_1$	$\Delta r_2/R_2$
Mesh 1	3λ	124	64	124	2.42×10^{-2}	4.16×10^{-3}	2.08×10^{-3}
Mesh 2	3λ	200	100	200	1.50×10^{-2}	2.63×10^{-3}	1.31×10^{-3}
Mesh 3	λ	200	100	200	5.0×10^{-3}	2.63×10^{-3}	1.31×10^{-3}

TABLE II. Characteristics of the different meshes used for the validation cases $\eta = 0.5$. Δx is the grid spacing along the axial direction and, Δr_1 and Δr_2 are the radial grid spacing at the inner and outer cylinder, respectively.

η	N_x	N_r	N_θ	$\Gamma = \lambda/(R_2 - R_1)$	Δx^+	$r\Delta\theta^+$	$\Delta r^+_{1,min}$	$\Delta r^+_{1,max}$	$\Delta r^+_{2,min}$	$\Delta r^+_{2,max}$
0.5	200	100	200	2.09	2.9	9	0.78	5.44	0.79	5.50
0.72	200	100	400	2.09	4.5	10	0.65	4.48	0.55	3.84
0.91	200	100	600	3.08	3.14	20	0.53	3.69	0.69	4.82

TABLE III. Description of meshes used for the computation of the flow (number of grid points in the three directions and grid spacing in terms of wall units for $Re = 5000$).

Finally, we report the comparison of our results with the correlation for the viscous torque

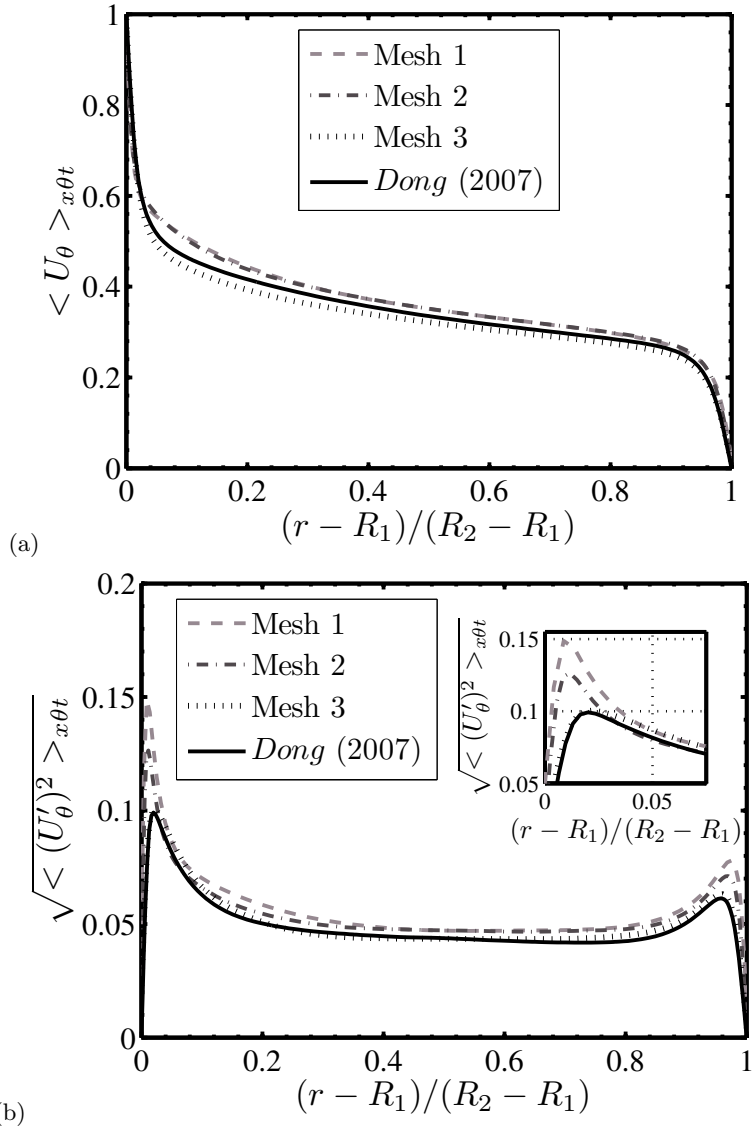

FIG. 3. Radial profiles of (a) the mean azimuthal velocity and (b) the azimuthal velocity fluctuation for different meshes compared to simulations of Dong[5] for $\eta = 0.5$ and $Re = 8000$.

T acting on the inner cylinder proposed by Wendt[35]. This correlation (see caption of fig. 4.a) gives an estimate of the dimensionless torque $G = T/\rho\nu^2 L_{ax}$ as a function of the Reynolds number and the radius ratio. Our results for the dimensionless average torque experienced by the inner cylinder compares favourably to the correlation of Wendt[35] as shown in fig. 4.a indicating that for our Reynolds number range, a power scaling $G \approx Re^{1.5}$ is a good compromise for the different radius ratios. Recent works[36,37] focused on the evolution of a Nusselt number Nu_ω for the general configuration where both cylinders can independently rotate. Nusselt number is defined for Taylor-Couette flows as the ratio between G and the dimensionless torque G_{lam} associated to pure Couette flow: $Nu_\omega = G/G_{lam}$. Ostilla et al.[36] observed a change in the local scaling for an approximate critical Taylor number $Ta \approx 3.10^6$ depending on the radius ratio. For small Reynolds numbers, they observed $Nu_\omega - 1 \approx Ta^{1/3}$ (i.e. $\approx Re^{2/3}$). For moderate Reynolds numbers, the scaling law shifts to $Nu_\omega - 1 \approx Ta^{0.2}$ (i.e. $\approx Re^{0.4}$). For high Reynolds numbers (Taylor numbers larger than 10^8), they obtained $Nu_\omega \approx Ta^{0.38}$ (i.e. $\approx Re^{0.76}$) referred as the ultimate regime

which does not depend on the radius ratio. In the range of Reynolds numbers we studied, Merbold et al.[37] proposed an evolution $Nu_\omega \approx Re^{0.62}$ very close to the scaling proposed by Ostilla et al.[36] for the small Reynolds regime. In our study, different power scaling laws were tested and we obtain a good agreement with the evolution $0.04Re^{0.617}$ as shown in fig. 4.a. The time evolution of the inner and outer torque has been used to determine if the permanent regime is reached (fig. 4.b). After a transient regime, the torques acting on the inner and outer cylinders finally converge to the same value (one percent overall variation for the evolution reported in fig. 4.b).

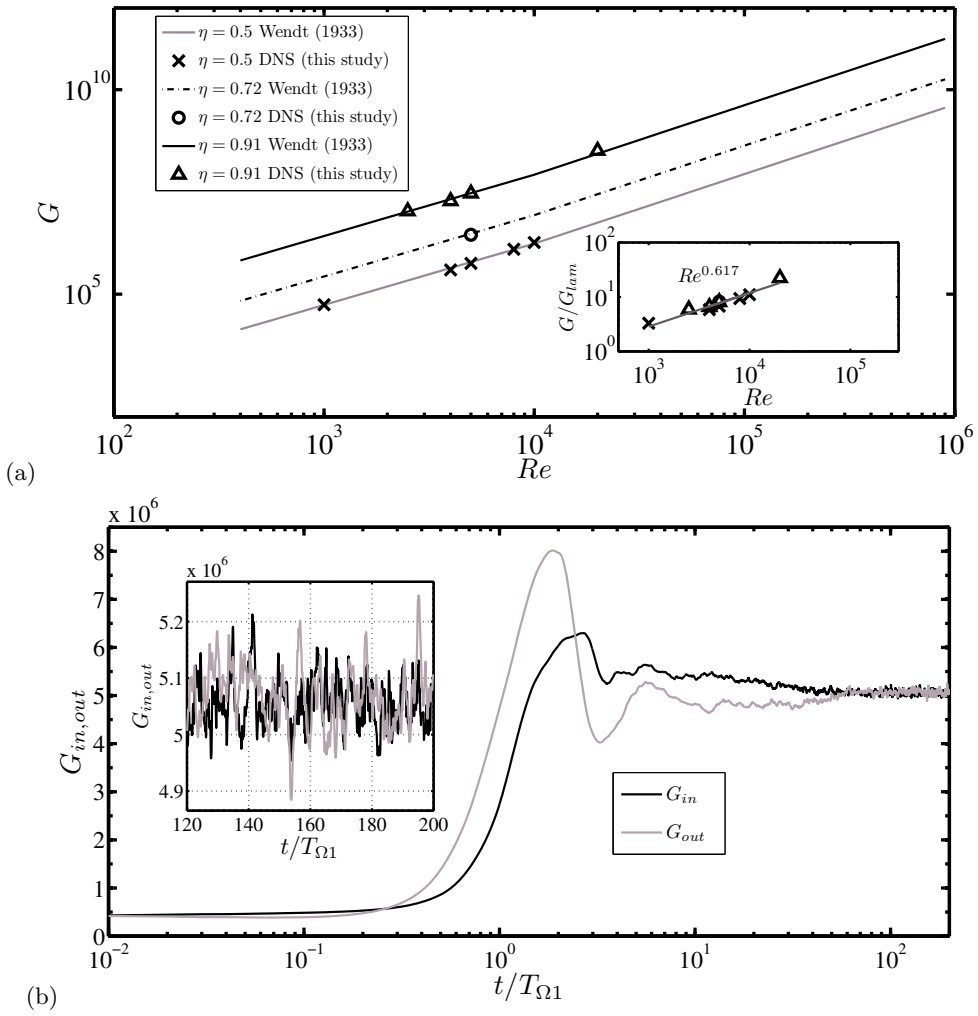

FIG. 4. (a) Comparison of dimensionless torque acting on the inner cylinder with the correlation[35] $G_{Wendt} = 1.45\left[\eta^{3/2}/(1-\eta)^{7/4}\right] Re^{3/2}$, and (inset) evolution of the Nusselt number $Nu_\omega = G/G_{lam}$ with Re, (b) Time evolution of the dimensionless torque acting on the inner and outer cylinders for $\eta = 0.72$ and $Re = 6000$

B. General structure of the flow

The TTVF regime is characterized by the development of turbulent structures and the persistence of the Taylor vortices. Isocontours of the fluid velocity highlight the presence of large scale Taylor vortices, that are modulated by small scale turbulent fluctuations (fig. 5).

The numerical study of Dong[5] showed that increasing the Reynolds number enhances small scale fluctuations. This can be clearly observed in fig. 6 for $\eta = 0.5$ and three different Reynolds numbers. Same features of the flow were observed for another gap ratio[6]. Figure 7 shows those structures in our simulations for the smallest gap configuration ($\eta = 0.91$). It is also important to remind that the circulation of the Taylor vortices induces the presence of inflow and outflow jets impacting on walls.

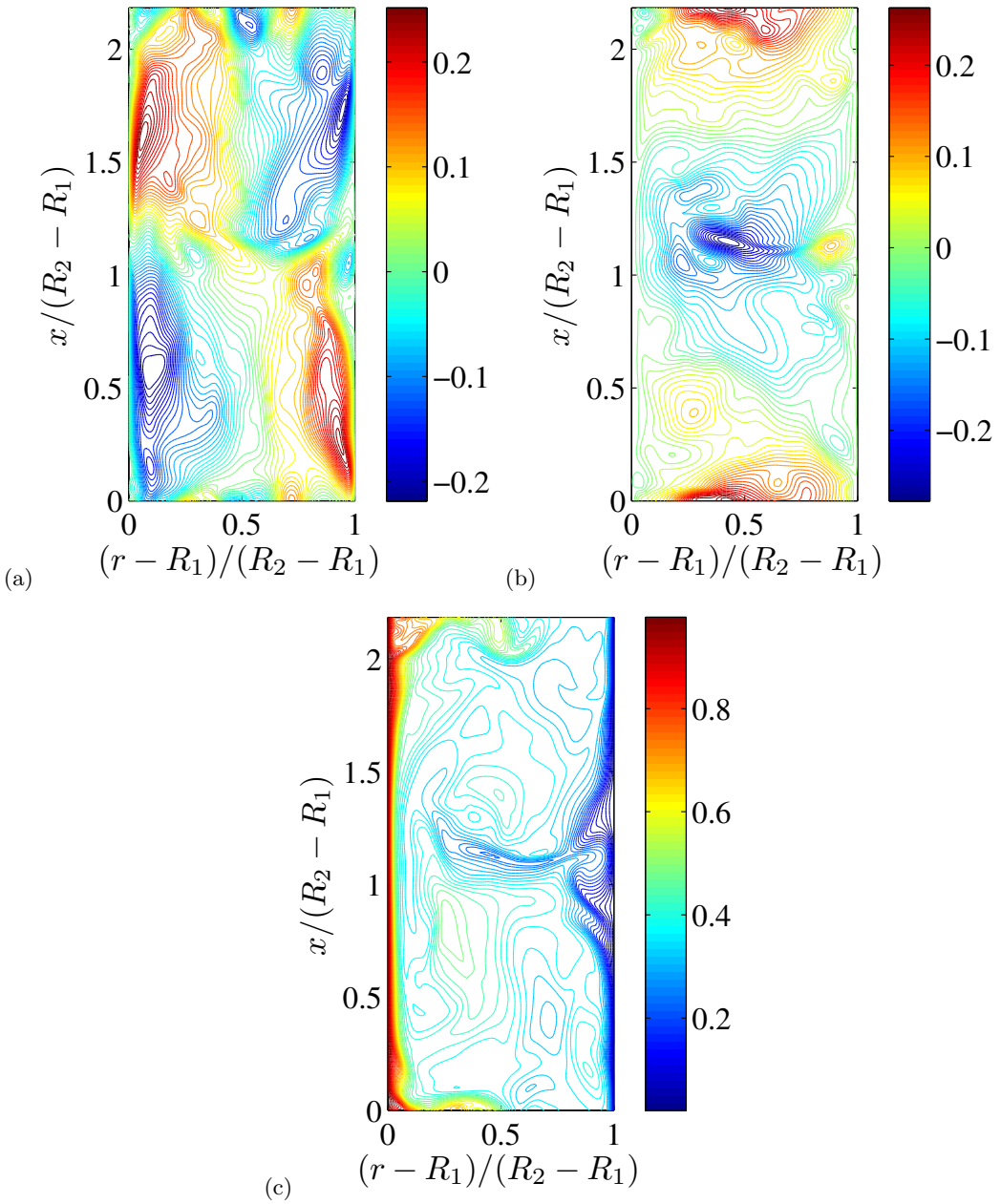

FIG. 5. Isocontours of the velocity for $\eta = 0.72$ and $Re = 5000$ in an axial-radial plane: (a) Axial, (b) radial and (c) azimuthal component (color on line).

The general trend of the azimuthal component is similar for different Reynolds numbers and radius ratios (fig. 8). Varying Re or η mainly changes the slope in the near wall region and the amplitude of the velocity in the bulk of the fluid. In order to discuss the different

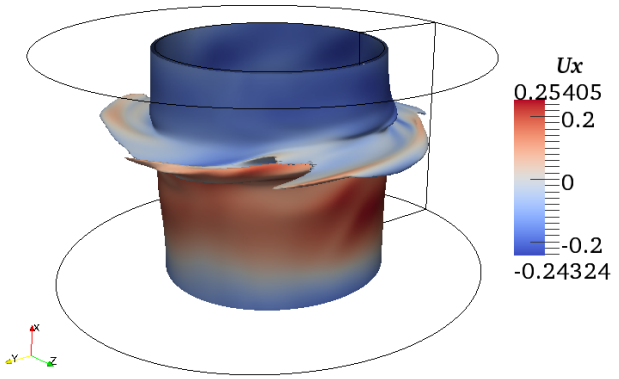

(a)

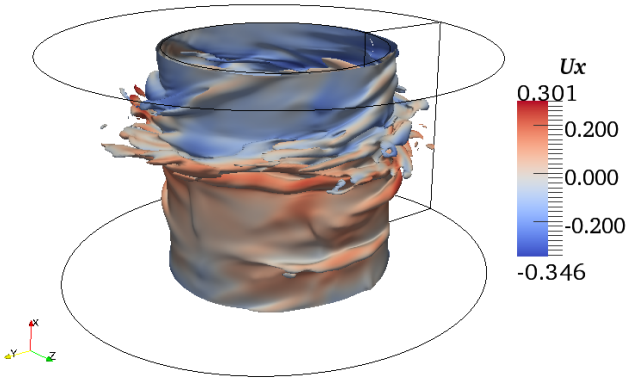

(b)

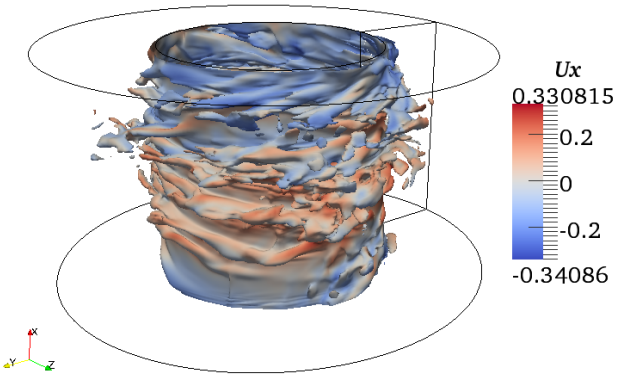

(c)

FIG. 6. Isocontour $|\mathbf{U}| = 0.5$ of the velocity for $\eta = 0.5$ and different Reynolds numbers: (a) $Re = 3000$, (b) $Re = 5000$, (c) $Re = 8000$. (color on line)

contributions of the velocity field, we introduce two different averaging procedures[6]. We use the notation $< \cdot >_{x\theta t}$ for an average calculated over the azimuthal and axial directions and time. The second one, $< \cdot >_{\theta t}$, corresponds to an average over the azimuthal direction and time only. Figure 9 presents isocontours of the velocity field $< \mathbf{U} >_{\theta t}$. It emphasizes the presence of large scale Taylor vortices. We also define two distinct fluctuations in order

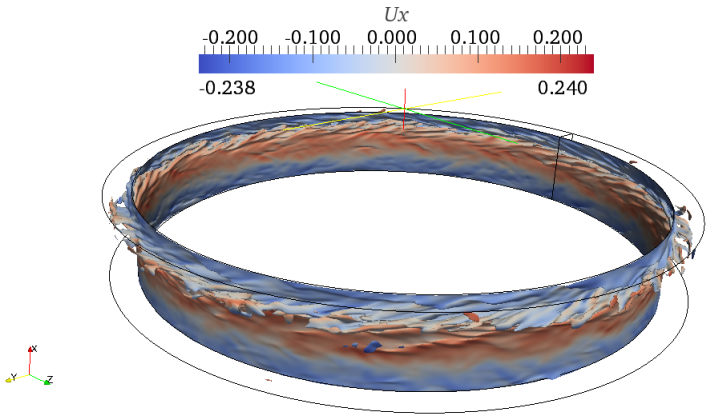

FIG. 7. Isocontour $|\mathbf{U}| = 0.6$ of the velocity for $Re = 5000$ and $\eta = 0.91$. (color on line)

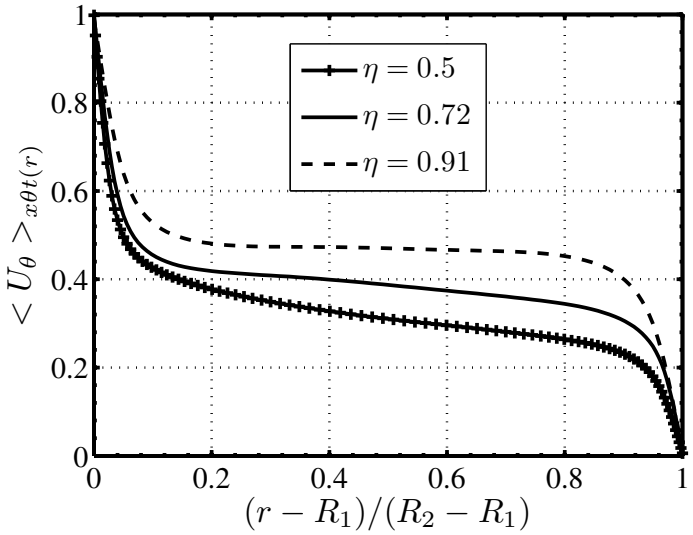

FIG. 8. Influence of the geometry on the azimuthal flow: radial evolution of the mean azimuthal velocity at $Re = 5000$ for different η.

to describe the turbulent contribution to the flow:

$$\mathbf{u}(x,r,\theta,t) = <\mathbf{u}>_{x\theta t}(r) + \mathbf{u}^{'}(x,r,\theta,t) \quad (4)$$

$$\mathbf{u}(x,r,\theta,t) = <\mathbf{u}>_{\theta t}(x,r) + \mathbf{u}^{''}(x,r,\theta,t) \quad (5)$$

Figure 10 shows the rms velocity profiles for the two averaging procedures. It appears that the fluctuations $u^{'}$ are more intense than $u^{''}$ which is consistent because Taylor vortices are accounted for in this definition of fluctuations. We also observe that the level of fluctuations $u^{''}$ increases with the Reynolds number, while the level of $u^{'}$ decreases. It implies that the relative importance of the Taylor vortices decreases with the Reynolds number in favor of the small scale fluctuations. The azimuthal component of $u^{'}$ fluctuations behaves similarly as observed in a turbulent channel flow: the fluctuation level decreases with the Reynolds number, and the maximum of fluctuating energy comes closer to the wall. For $Re \geq 5000$, the maximum of fluctuations is located at a distance from the inner wall $r_1^+ \approx 10$, which is slightly closer to the wall than for turbulent channel flows. The amplitude of the maximum

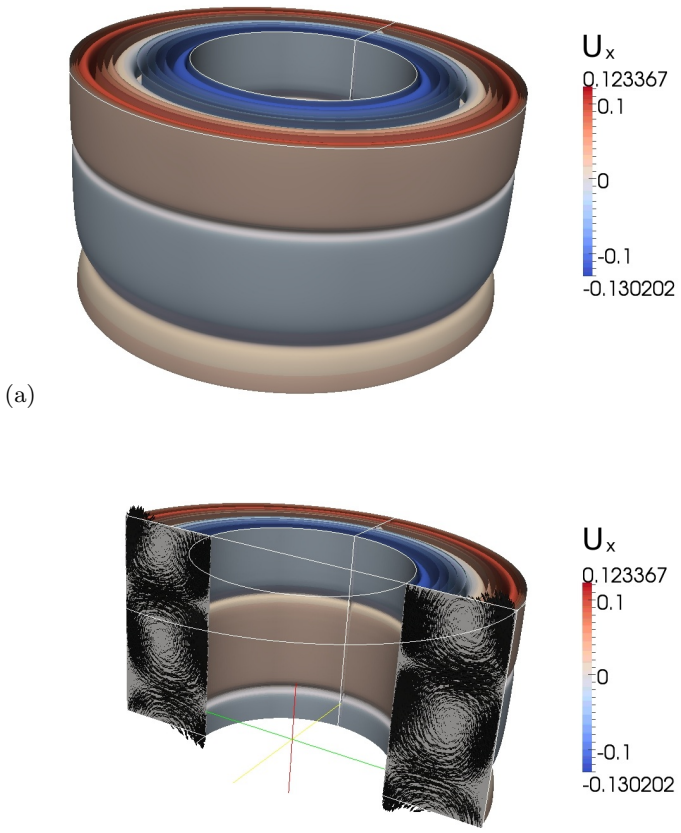

FIG. 9. Isocontours of the mean velocity field $< \mathbf{U} >_{\theta t}$ for $\eta = 0.5$ and $Re = 5000$ (colors correspond to axial velocity)

of $u_\theta^{'}$ is of the same order as turbulent channel flow values[38]. For $Re = 3000$, our results are in very good agreement with those of Bilson & Bremhorst[6] obtained for $Re = 3200$ and $\eta = 0.62$. The azimuthal fluctuations exhibit a maximum near the wall, $(u_\theta^{'})^{max} \approx 2u_1^*$ and $(u_\theta^{''})^{max} \approx u_1^*$, respectively (see next section for the definition of friction velocity u_1^* and wall units).

C. Description of the near wall region

We focus on the evolution of the velocity field in the near-wall region. The friction velocity is defined for each wall ($i = 1$ for inner cylinder and $i = 2$ for outer cylinder) $u_i^* = \sqrt{|\tau_{w,i}|/\rho}$, where $\tau_{w,i}$ is the wall shear stress[4,6]. We also introduce the corresponding viscous length-scale $\delta_i^* = \nu/u_i^*$. The balance of the total shear stress τ_{tot} averaged in the axial and azimuthal directions is given by

$$\tau_{tot}(r) = \rho\nu r \frac{\partial(< u_\theta >_{x\theta t} /r)}{\partial r} - \rho < u_\theta^{'} u_r^{'} >_{x\theta t} = \frac{cte}{r^2} \tag{6}$$

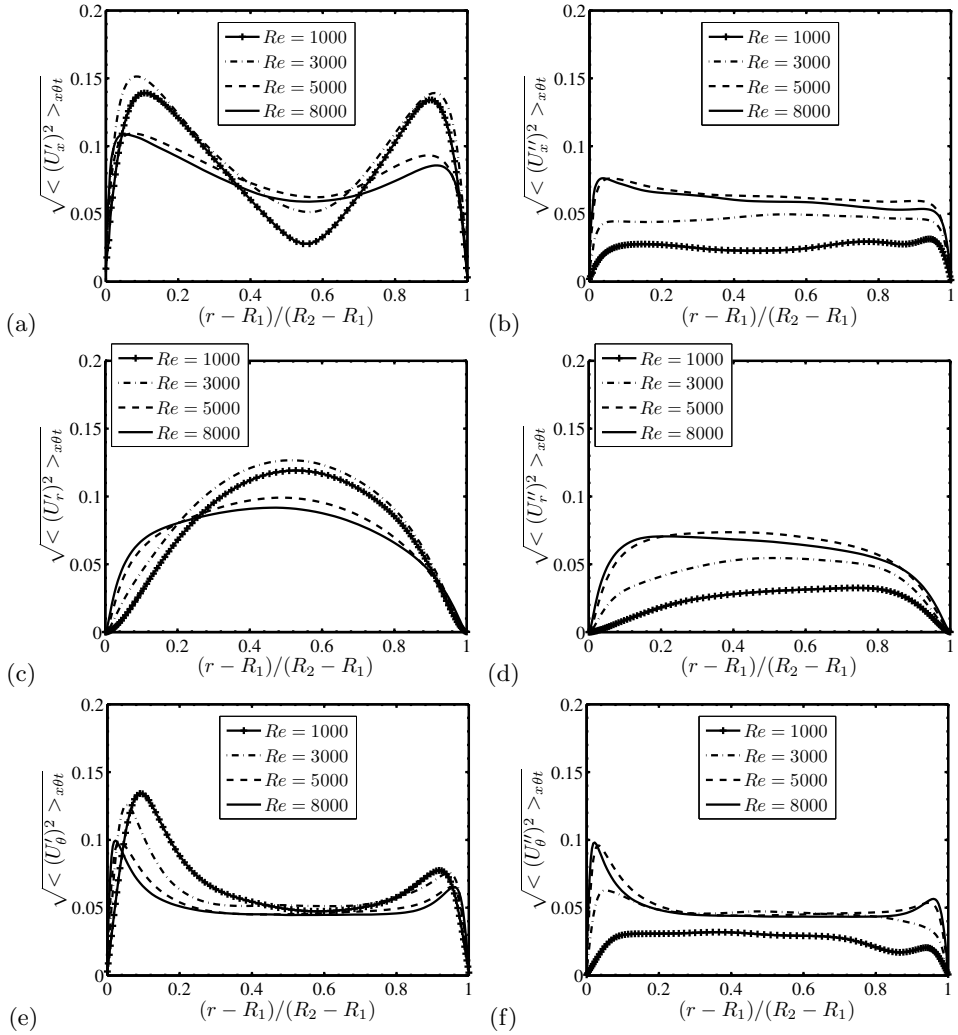

FIG. 10. Profiles of the root mean square velocity fluctuations for the two averaging procedures, for $\eta = 0.5$ and for different Reynolds numbers.

This is consistent with the conservation of the mean transverse angular momentum[39] leading to equality of the torques applied on the inner and outer cylinders. Turbulent shear stress is negligible in the near wall region, so that eq. 6 can be rewritten in the near-wall regions as:

$$\rho\nu r\frac{\partial(< u_\theta >_{x\theta t}/r)}{\partial r} = \frac{cte}{r^2} = \frac{\tau_{w1}R_1^2}{r^2} = \frac{\tau_{w2}R_2^2}{r^2}. \tag{7}$$

Assuming $r \approx R_i$ close to the corresponding wall, it follows from the integration of eq. 7 a linear evolution for the inner and outer velocities $u_i = U_i - < u_\theta >_{x\theta t}$ normalized by the friction velocity:

$$u_i^+ = \left(1 + \frac{U_i\delta_i^*}{R_i u_i^*}\right) r_i^+, \tag{8}$$

An estimate based on the Wendt's correlation[35] of the ratio $U_1\delta_1^*/R_1u_1^*$ indicates that this term is much smaller than 1 for $Re > 2000$, so that the approximation $U_1 - < u_\theta >_{x\theta t} \approx \frac{{u_1}^*}{{\delta_1}^*}(r - R_1)$ can be made. Indeed, we show in fig. 11 a linear evolution on

both walls similar to turbulent channel flows. Similar trends were observed numerically[6,40], and experimentally[41]. It confirms the existence of an inner layer of constant shear stress where viscous diffusion is prevailing and curvature effect is negligible. It is worth noting that for $Re > 5000$, profiles are well superposed with this linear evolution indicating that ${u_i}^*$ and ${\delta_i}^*$ are the characteristic velocity and length scales of the flow in near wall regions, respectively.

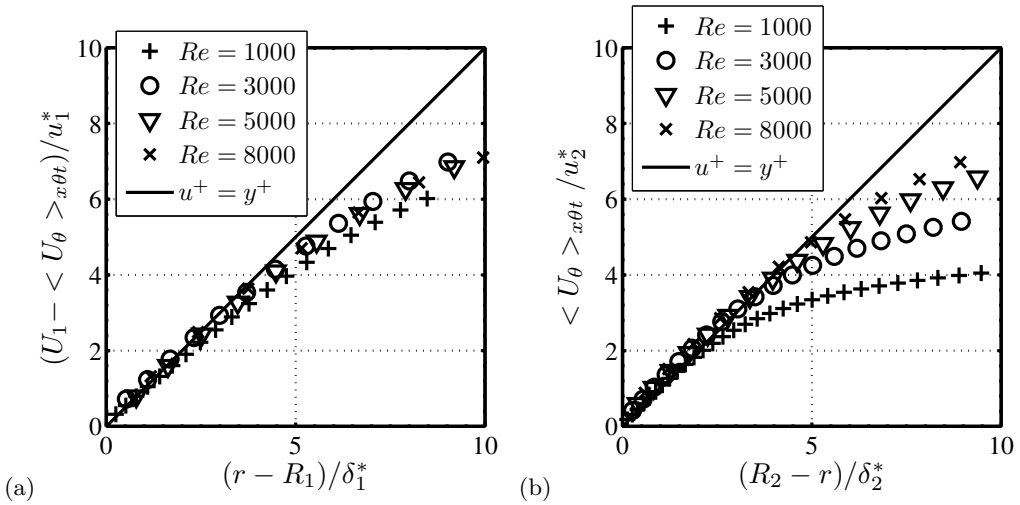

FIG. 11. Evolution of the mean azimuthal velocity normalized by the friction velocity for different Reynolds numbers ($\eta = 0.5$). Wall normal distances are reported in wall units (a) near the inner cylinder and (b) near the outer cylinder. The linear law $u^+ = y^+$ is reported in solid line for comparison (y^+ stands for the normalized distance normal to a cylinder).

As in turbulent channel flows, one can define a turbulent Reynolds numbers for each cylinder i as $Re_i^* = u_i^*(R_2 - R_1)/\nu$. Their values are reported in Table IV. The study

Re	Re_1^*	Re_2^*
1000	94.27	47.24
3000	200.1	99.6
5000	300.2	150.8
8000	446.6	223.0

TABLE IV. Values of the inner- and outer- turbulent Reynolds numbers and for different Reynolds numbers ($\eta = 0.5$).

performed in the high Reynolds number regime[41] highlighted a linear evolution of the normalized azimuthal velocity similar to the $u^+ = y^+$ evolution observed for a turbulent channel flow (where y^+ is the dimensionless distance to the wall) and a logarithmic behavior for $y^+ > 30$. This linear evolution has also been numerically observed for smaller Reynolds numbers ($Re \approx 10^3$)[6,40], but the logarithmic evolution was not observed for Re^* between 340 and 380[40].

Further from the wall, we have tested the validity of a logarithmic law (fig. 12) using the same fitting range as in the work of Huisman[42] ($y^+ > 50$). The slope is expected to be different from the results of Smith and Townsend[41] obtained for larger Reynolds numbers ($Re \approx 21000 - 50000$). Indeed, the ratio $(R_2 - R_1)/\delta_1^*$ is close to 400 for our larger Reynolds number $Re = 8000$ while it is larger than 1000 in their experiments. Thus, we expect that the boundary layers attached to each cylinder are still interacting for the Reynolds numbers we considered, explaining why we did not observe a log-law with the Von Kàrman constant. We observe a law $log(y^+)/B$ with B varying from 1.37 for $Re = 3000$ to 0.68 for $Re = 8000$. This decrease of B when increasing Re is consistent with the

experimental works of Huisman[42], for which $B \simeq 1.6$ at the inner wall for $Re \simeq 5000$. They observe that B asymptotically approaches to the Von Kàrman constant for high Re. Recent works of Grossmann et al.[43] highlighted that log-law with a Von Kàrman constant is more appropriate for the radial evolution of the angular velocity ω than for the azimuthal velocity. The evolution of the angular velocity is presented in fig. 12.b . The constant $B^{'}$ associated with angular velocity profiles varies from 0.71 for $Re = 3000$ to 0.45 for $Re = 8000$. Enhanced universality of the log-law is achieved with the angular velocity than with the azimuthal velocity.

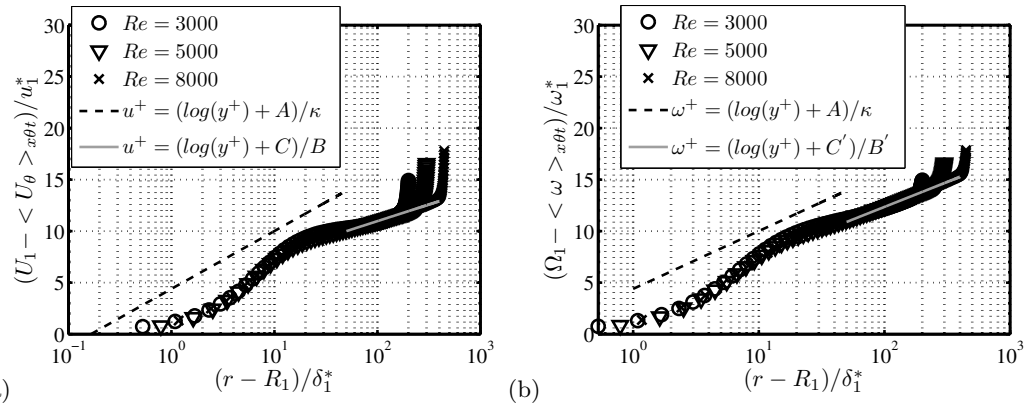

FIG. 12. Evolution of the mean velocity (a) and angular velocity (b) normalized by the friction velocity and angular velocity ($\omega_1^* = u_1^*/R_1$) respectively for different Reynolds numbers ($\eta = 0.5$). Wall normal distances are scaled using wall units, both figures correspond to the inner cylinder boundary layer. A log-law with $\kappa = 0.41$ and $A = 1.8$ is shown for comparison in dashed line. Best fit near the inner cylinder for all Re is represented in grey, it corresponds to $B = 0.71$ and $C = 3.23$ for azimuthal velocity and $B^{'} = 0.48$ and $C^{'} = 1.26$ for the angular velocity

III. BUBBLE DISPERSION

A. Lagrangian tracking

The dispersed phase is composed of N_b clean spherical bubbles. Bubble trajectories are computed by time integration of the force balance, which accounts for buoyancy, drag, pressure gradient, added mass and lift forces. For each bubble of radius R_b (and volume $\mathcal{V}_b$), velocity $\mathbf{v}$, the force balance can be written as a function of the velocity of the fluid $\mathbf{u}$ at the bubble location and its gradients:

$$\rho_b \mathcal{V}_b \frac{d\mathbf{v}}{dt} = (\rho_b - \rho_f)\mathcal{V}_b \mathbf{g} - \rho_f \mathcal{V}_b \frac{3}{8R_b} C_D |\mathbf{v} - \mathbf{u}|(\mathbf{v} - \mathbf{u}) + \rho_f \mathcal{V}_b \frac{D\mathbf{u}}{Dt} + \rho_f \mathcal{V}_b C_M \left[\frac{D\mathbf{u}}{Dt} - \frac{d\mathbf{v}}{dt}\right] - \rho_f \mathcal{V}_b C_L (\mathbf{v} - \mathbf{u}) \times \mathbf{\Omega} \quad (9)$$

The bubble Reynolds number is defined as

$$Re_b = \frac{|\mathbf{u} - \mathbf{v}|\, 2R_b}{\nu} \quad (10)$$

The added-mass coefficient for a spherical object[44] is equal to $C_M = 1/2$. The drag coefficient is given by[45]:

$$C_D = \frac{16}{Re_b}\left[1 + \left(\frac{8}{Re_b} + \frac{1}{2}\left(1 + \frac{3.315}{Re_b^{1/2}}\right)\right)^{-1}\right] \quad (11)$$

This correlation obtained thanks to DNS around a spherical bubble describes the drag coefficient whatever its Reynolds number. The lift coefficient is given by[25]:

$$C_L = \left[\left(\frac{2.2555 \times 6/\pi^2}{(1 + 0.2(|\mathbf{v} - \mathbf{u}|^2/S\nu))^{3/2}} \left(\frac{\nu}{S d_b^2} \right)^{\frac{1}{2}} \right)^2 + \left(\frac{1}{2} \frac{1 + 16/Re_b}{1 + 29/Re_b} \right)^2 \right]^{\frac{1}{2}} \tag{12}$$

which depends on the bubble Reynolds number and on the local shear rate intensity $S = 2R_b \|\mathbf{\Omega}\| / \|\mathbf{u} - \mathbf{v_b}\|$. It has been shown that the force balance (9) combined with the added mass, drag and lift coefficients given above is able to correctly describe the force acting on a clean spherical bubble in a turbulent flow[46] .

Periodic conditions are imposed for the bubble trajectories at the upper and the bottom of the domain while an elastic bouncing is imposed on the inner and outer walls. The time integration of the force balance (9) is carried out for each bubble with a second-order Runge-Kutta scheme. For each time step of the temporal solution of Navier-Stokes equations, several time steps of the force balance integration are required. Indeed, Lagrangian tracking has its own time constraint $dt \approx \tau_b/5$ where $\tau_b = R_b^2/6\nu$ is the bubble relaxation time. The fluid velocity as well as its spatial and time gradients need to be evaluated at the bubble location. Those Lagrangian quantities are interpolated with second order accuracy. The Lagrangian tracking has been widely used and validated[47,48]. For the present study, parallel computing of the Lagrangian equations was necessary in order to simulate large amount of bubbles, typically $N_b = O(10^6)$. When the flow has reached a statistical steady state for the considered Reynolds number, bubbles are seeded at random initial positions with velocity equal to the fluid velocity at the bubble locations.

The force balance used in the simulations is only valid for spherical bubbles. We validated this hypothesis *a posteriori* by measuring the bubble Weber number based on the instantaneous slip velocity or based on the turbulence fluctuations. Considering fluid properties corresponding to classic air/water systems, both Weber numbers were found to be much smaller than unity (typically lower than 10^{-2}).

B. Dispersion of bubbles in non-turbulent Taylor-Couette flows.

Climent et al.[23] proposed to consider two dimensionless parameters H and C to characterize the major migration mechanisms in Taylor vortex flows. Migration is dominated by three main effects: (i) the azimuthal rotation of the inner cylinder induces attraction towards the inner cylinder, (ii) the flow circulation within Taylor Vortices generates entrapment of bubbles in the vortex cores and (iii) buoyancy effects yield bubble rising through the flow structures. These effects are compared throughout the dimensionless parameters H and C:

$$C = U_{TV}/V_T \tag{13}$$

$$H = 4 \left(\frac{U_{TV}}{U_1} \right)^2 \frac{R_1}{R_2 - R_1} \tag{14}$$

where U_{TV} corresponds to a characteristic velocity of the Taylor Vortices and V_T stands for the terminal velocity of the bubbles. Depending on the evolution of the (H, C) parameters, the following migration scenarii have been observed for Taylor vortex flows[23]. Accumulation in the axial direction can be explained as follows: a large value of parameter C implies small buoyancy effects and bubbles can be trapped within toroidal Taylor Vortices. On the contrary for small C values, related to high buoyancy effects, bubbles rise through the flow. Radial accumulation is then described using H parameter: a high H value indicates that bubbles are trapped in Taylor vortices, while a low value indicates that accumulation towards the inner cylinder is dominant. Three main scenarii are then obtained: for large C

and H values bubbles are trapped within the Taylor vortices, for a large C and a small H bubbles are attracted towards the inner cylinder and accumulate preferentially in outflow regions, and finally for small C and large H values bubbles accumulate uniformly along the inner cylinder. It is important to note that C depends on both the characteristics of the carrier flow and the bubbles, while H only depends on the characteristics of the flow.

The aim of this section is to study the relevance of these parameters on bubble dispersion for the turbulent regime. The evolution of H depending on the radius ratio and the Reynolds number is shown in fig. 13 for several geometric configurations. For turbulent flows, those dimensionless parameters are evaluated on the large-scale contributions of the flow. Two estimates of the characteristic velocity of Taylor Vortices U_{TV} are shown for both radial and axial components. They give the same general trends: a decrease of H with the Reynolds number, and an increase of H for increasing η which implies that reducing the gap width should promote accumulation in Taylor Vortices. As discussed in the next section, this conclusion will be modulated by the presence of small-scale turbulent structures which tend to disperse bubbles throughout the gap between the cylinders.

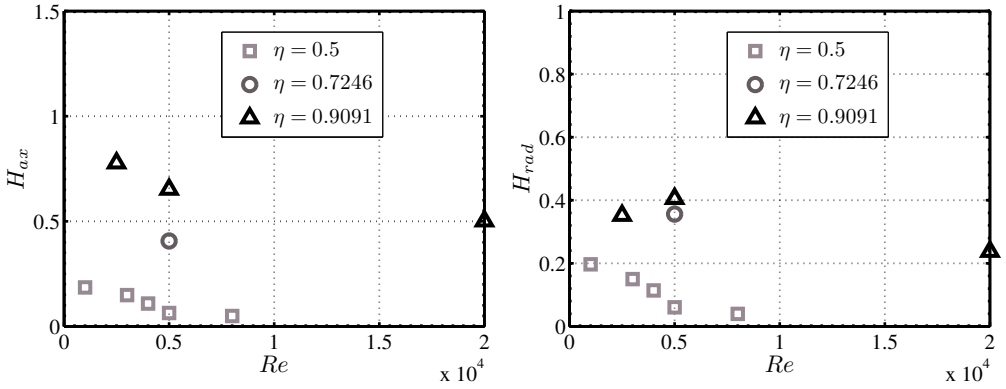

FIG. 13. Values of the parameter H for different Reynolds numbers and different radius ratios corresponding to this study. The estimate of U_{TV} is based on (left) the computed axial component of Taylor Vortices and (right) on their radial component.

Table V reports the two-phase flow configurations we simulated. We are aiming to study the influence of the Reynolds number (through H variation), the bubble size by changing R_b/R_2, and the role of buoyancy effects by considering two different values of C. In experiments, these effects can hardly be tested independently since C depends both on gravity and bubble size (bubble size is controlled by the injection flow rate, the nozzle geometry and possibly the local shear rate which in turn depends on the flow Reynolds number). For all configurations the dispersed phase is composed of one million bubbles, but figures representing bubble positions display only 20000 bubbles in order to ease visualizations (typically fig. 14). Table V also gives an estimate of the Stokes numbers based on the characteristics of the inner cylinder wall turbulent scales $St = \tau_b/(\delta_1^*/u_1^*)$. Our analysis is organized as follows: we will first present the general arrangement of the dispersed phase and the corresponding void fraction profiles. We will focus on cases without gravity effects ($\mathbf{g} = \mathbf{0}$). Then, we describe the effect of gravity by varying C and finally we discuss the effects of the flow Reynolds number Re and the bubble size R_b/R_2.

C. Bubble accumulation without gravity effects

We first consider dispersion for case 1 corresponding to the largest bubbles considered with $g = 0$ ($C = \infty$), for $Re = 5000$ and $\eta = 0.5$ (see Table V). Bubble positions for successive times are presented in fig. 14. We observe for short times that most of the bubbles are transported from the outflow region towards the outer cylinder. Strong

Case	Re	R_b/R_2	$(R_2-R_1)/2R_b$	$2R_b/\delta_1^*$	H	C	St_1
1	5000	2.10^{-3}	125	2.32	0.0637	∞	0.23
2	5000	2.10^{-4}	1250	0.23	0.0637	∞	0.0023
3	3000	2.10^{-3}	125	1.5068	0.1490	∞	0.0946
4	5000	2.10^{-3}	125	2.32	0.0637	0.5	0.23
5	5000	2.10^{-4}	1250	0.23	0.0637	0.5	0.0023

TABLE V. Parameters of the dispersed phase and the carrier flow presented in this study. The geometrical configuration corresponds to $\eta = 0.5$. The number of bubbles is $N_b = 10^6$.

dispersion of bubbles follows. The rest of bubbles is attracted towards the inner cylinder. For longer simulation times, bubbles are either concentrated in accumulation zones in the outflow region near the inner wall, or dispersed throughout the entire gap without any specific organization. The general trend is different for smaller bubbles (case 2) under the same H and C conditions (see fig. 15). We observe similar initial ejection at short times from the outflow region, but we do not observe any organization for longer times, neither in the gap nor in the near wall region of the inner cylinder. For cases with smaller Reynolds numbers (larger H value), large bubbles behave similarly (fig. 16): bubbles are initially ejected from the outflow regions and then dispersed in the flow, then attracted towards the inner cylinder and form collars in the outflow region. Therefore variations of H in the range of parameters we tested does not have a significant effect on the overall behavior of the dispersed phase.

Focusing on bubbles located in the near-wall region, we do not observe any specific arrangement for small bubbles (case 2). On the contrary, the arrangement for larger bubble (cases 1 and 3) is strongly affected by the local flow structures as shown in fig. 17, for both Reynolds numbers. Indeed, bubbles are trapped in the herringbone-like structures close to the inner cylinder, more precisely in high speed streaks corresponding to strong ejection of high momentum fluid. Despite the analogies with turbulent channel flow discussed in section II, the Taylor-Couette configuration exhibits original structures like the herringbone-like streaks[7] near the inner cylinder wall (so called Görtler vortices). These structures have also been observed near the outer cylinder[49], and then numerically evidenced on both cylinders[8]. Increasing the Reynolds number also increases the number of herringbone-like streaks in this inflow-outflow regions[8]. More recently simulations at higher Reynolds numbers ($Re \approx 30000$) highlighted again the presence of these herringbone-like streaks[50]. We show here that depending on the bubble size, these structures can have a significant effect on bubble preferential accumulation in the vicinity of the wall.

D. With gravity effects

The effect of gravity is now discussed by considering the case $C \approx 0.5$: the terminal rising velocity of the bubbles is almost half of the characteristic velocity of Taylor vortices. We remind that periodic boundary conditions are used for the bubble and the flow equations, so that bubbles reaching the upper boundary are re-injected at the bottom of the domain with the same velocity and acceleration. Compared to case $C = \infty$ ($g = 0$), we observe a different response of the bubbly phase. The influence of the outflow jet is less pronounced as shown in fig. 18 and fig. 19 for both bubble size (cases 4 and 5, respectively). Initial ejection by the outflow jet is now weaker, which confirms that Taylor vortices have less influence and that bubble migration in the vertical direction is dominated by buoyancy. In the radial direction, bubbles are attracted towards the inner cylinder, as expected. For larger bubbles, the spatial arrangement does not match herringbone-like streaks but forms well defined spirals as shown in fig. 20. These spirals could be related to bubbly spiral patterns observed experimentally[19] and reported in fig. 21. We estimated the value of C in these experiments and we found that our cases with $C \approx 0.5$ should correspond in the experimental study to Reynolds numbers between $Re = 600$ and $Re = 900$, which is

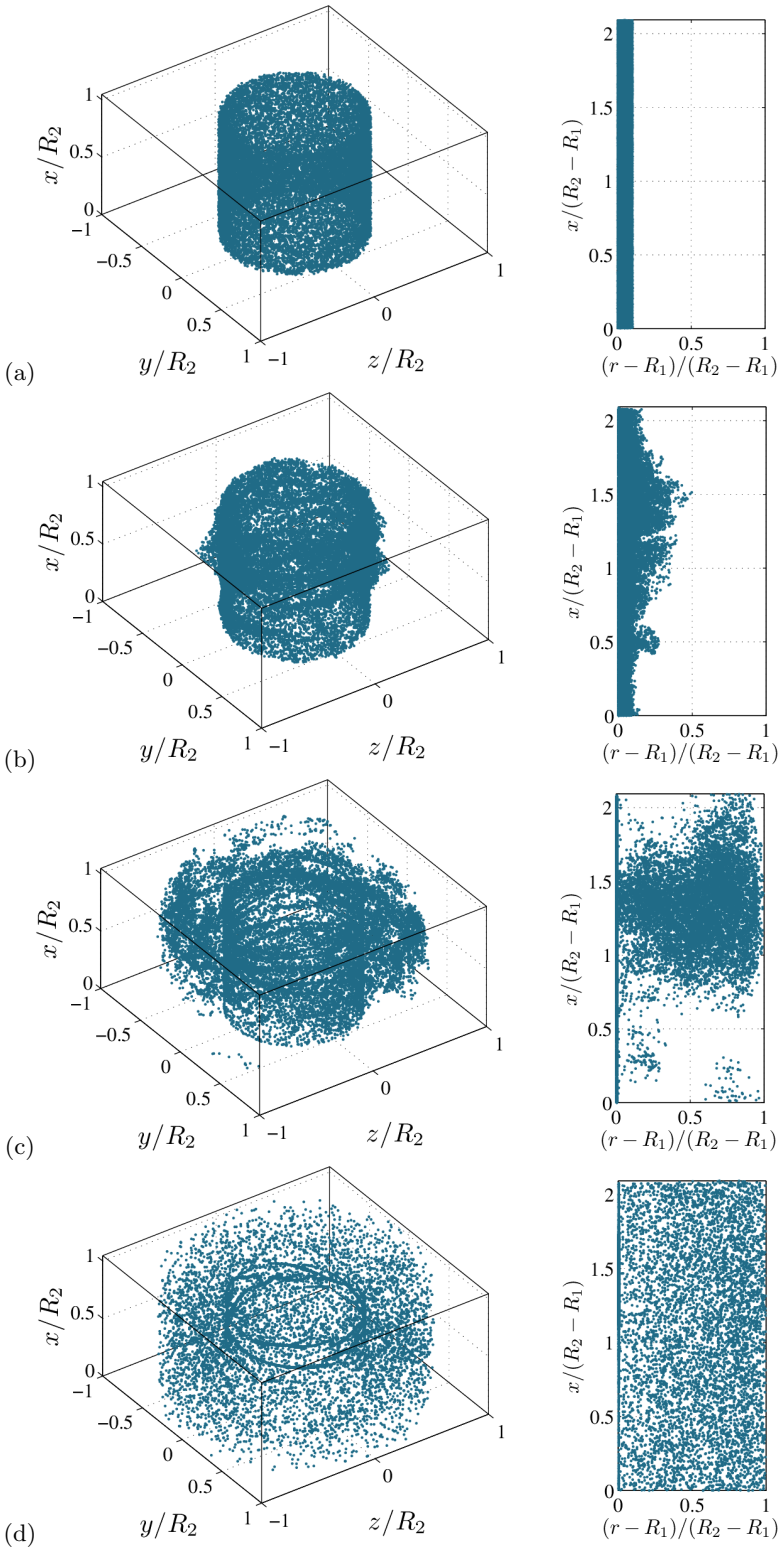

FIG. 14. Bubble positions (3D positions and projection in a $(\mathbf{e_r}, \mathbf{e_x})$ plane) at different times for case 1: (a) Initial positions - (b) after $0.2T_{\Omega 1}$ - (c) after $1.1T_{\Omega 1}$ - (d) after $19T_{\Omega 1}$

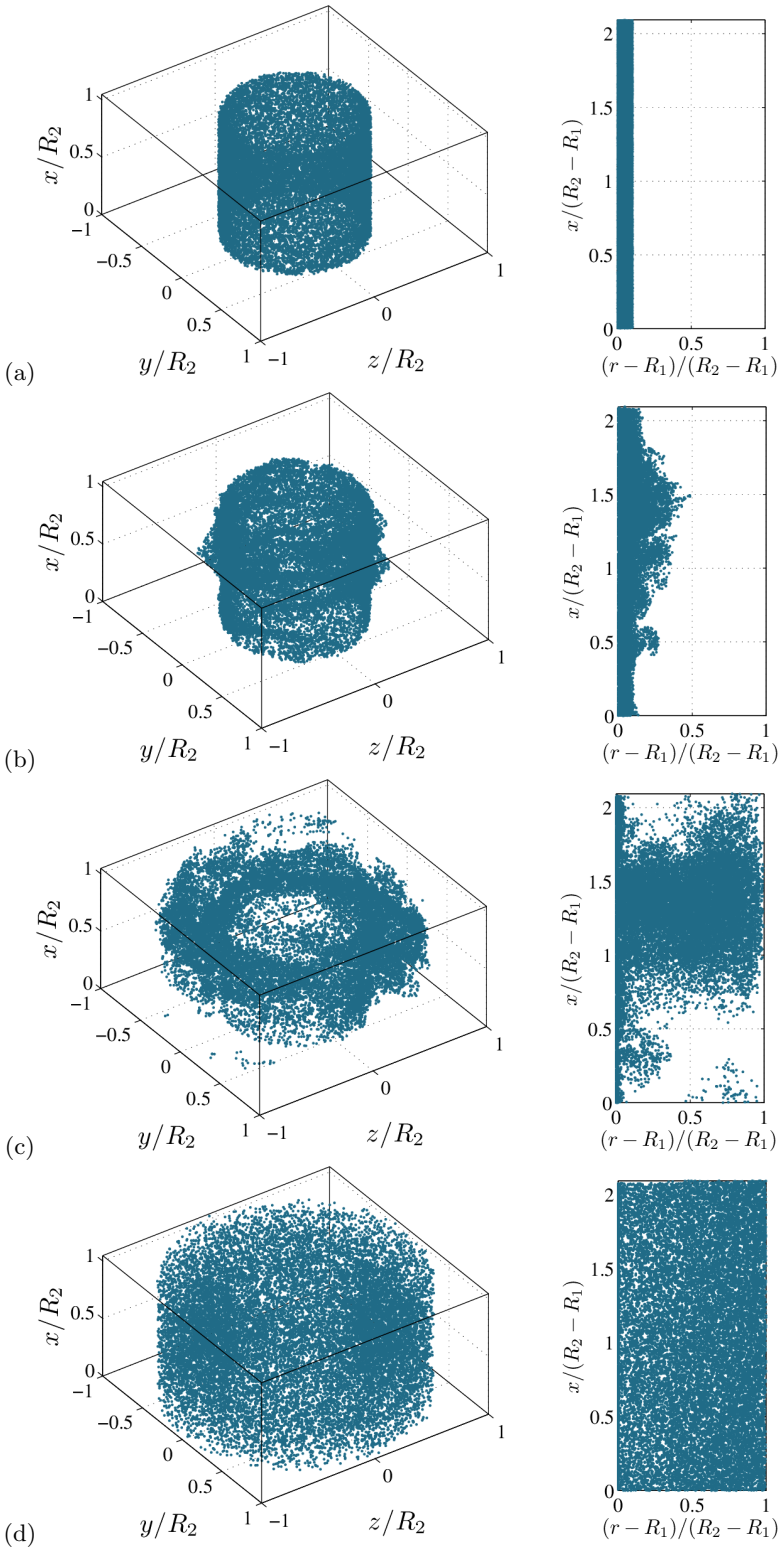

FIG. 15. Bubble positions (3D positions and projection in a $(\mathbf{e_r}, \mathbf{e_x})$ plane) at different times for case 2: (a) Initial positions - (b) after $0.2T_{\Omega 1}$ - (c) after $1.2T_{\Omega 1}$ - (d) after $10.5T_{\Omega 1}$

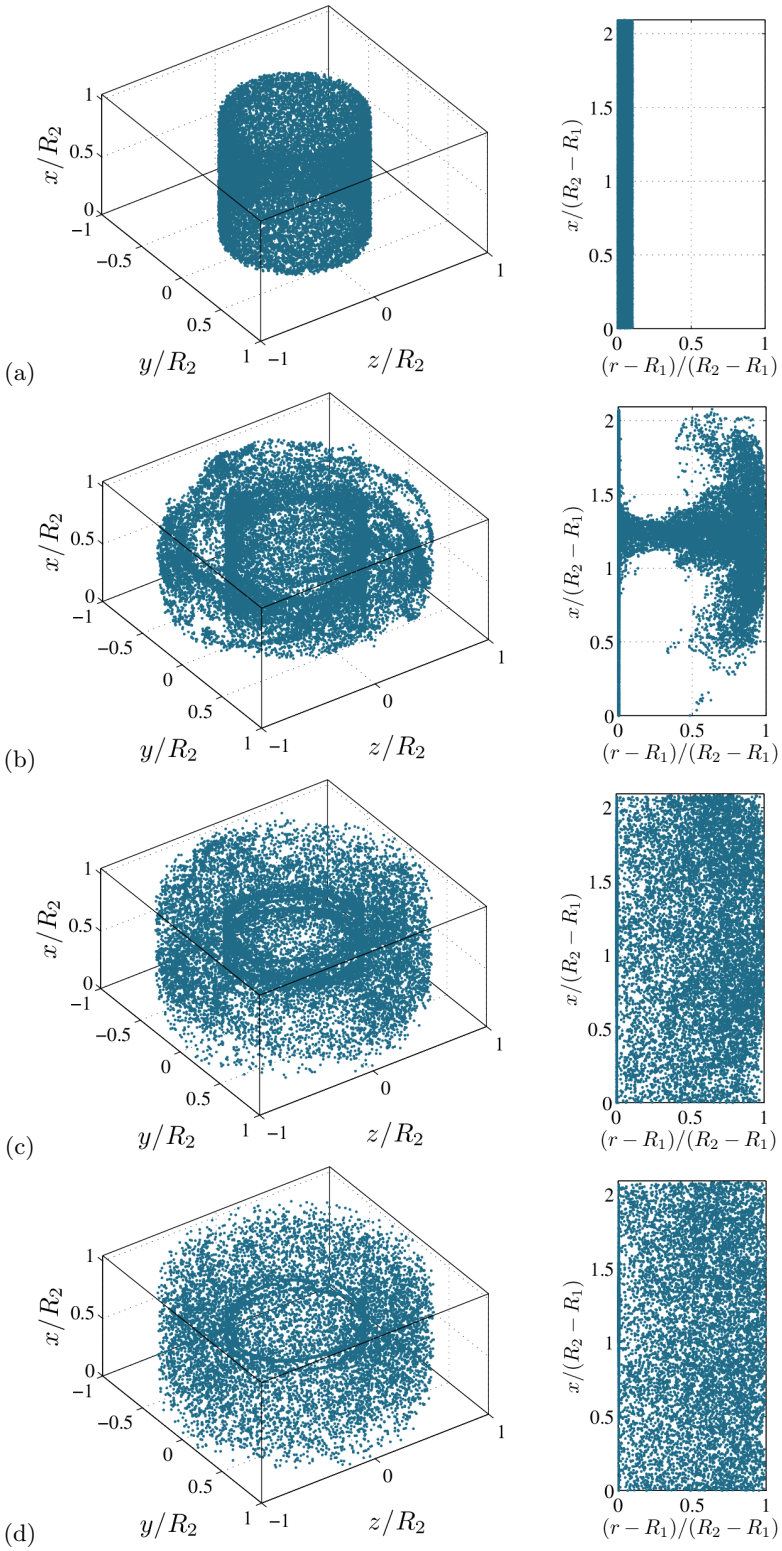

FIG. 16. Bubble positions (3D positions and projection in a $(\mathbf{e_r}, \mathbf{e_x})$ plane) at different times for case 3: (a) Initial positions - (b) after $T_{\Omega 1}$ - (c) after $4T_{\Omega 1}$ - (d) after $14T_{\Omega 1}$

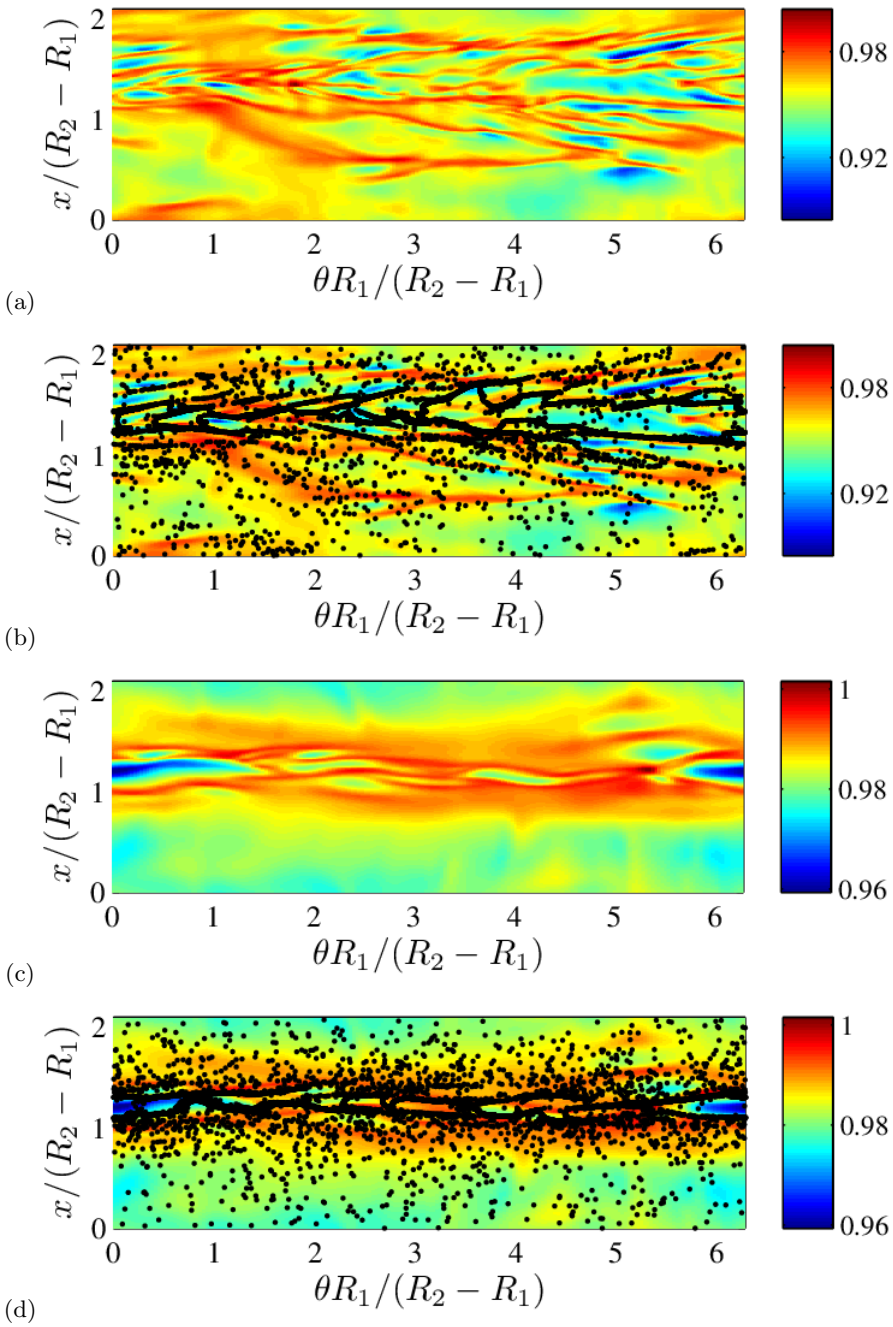

FIG. 17. Isocontours of the velocity and bubbles position in the near wall region for (a,b) $Re = 5000$ at $r_1^+ = 0.19$ (case 1) and (c,d) $Re = 3000$ at $r_1^+ = 0.11$ (case 3)

consistent with the accumulation patterns observed. Smaller bubbles (case 5 in fig. 19) seems to accumulate uniformly along the inner wall and we do not notice the formation of bubbly spirals in this region (fig. 20).

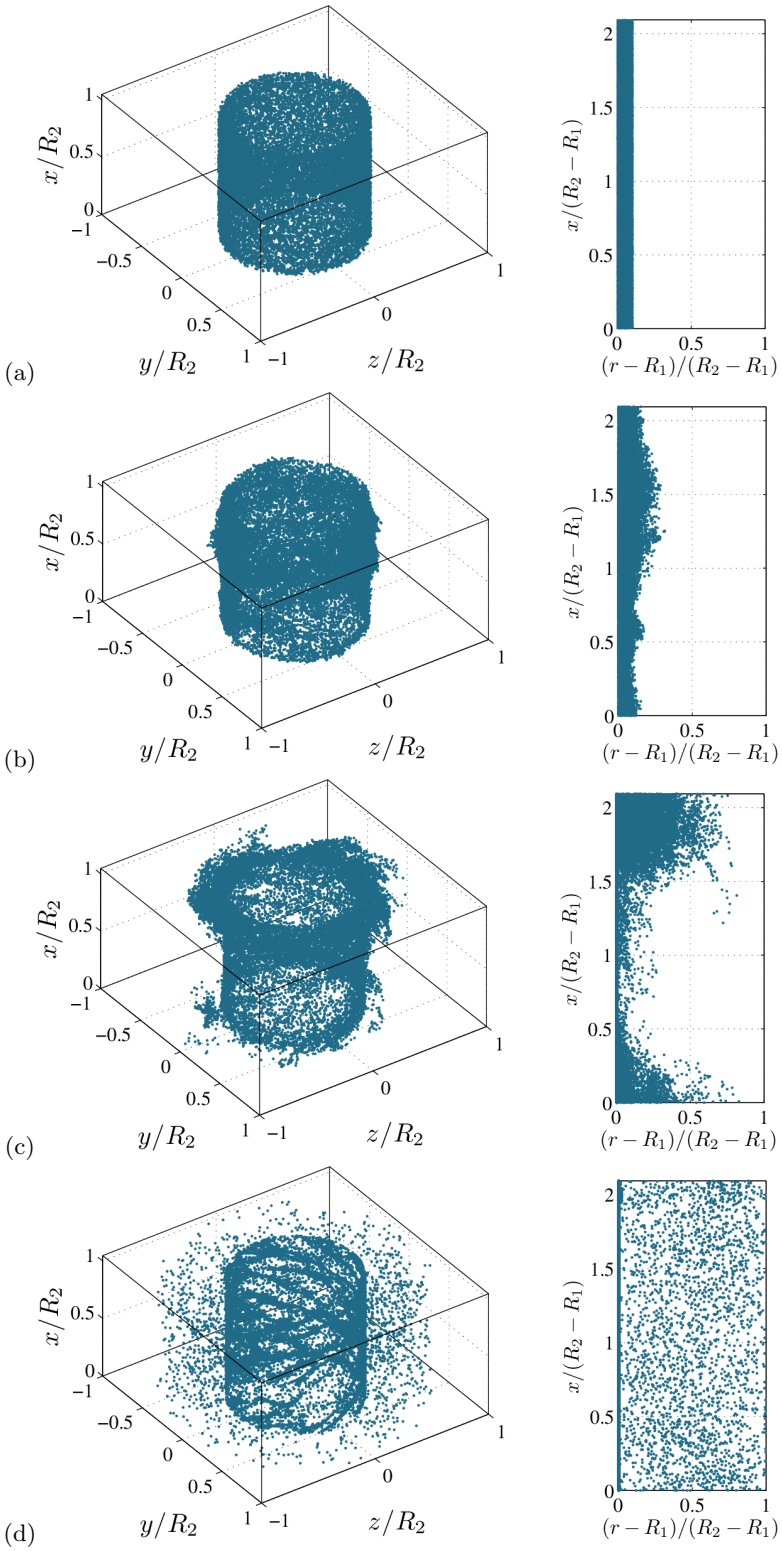

FIG. 18. Bubble positions (3D positions and projection in a $(\mathbf{e_r}, \mathbf{e_x})$ plane) at different times for case 4: (a) Initial positions - (b) after $0.2T_{\Omega 1}$ - after $1.1T_{\Omega 1}$ - (d) after $19T_{\Omega 1}$

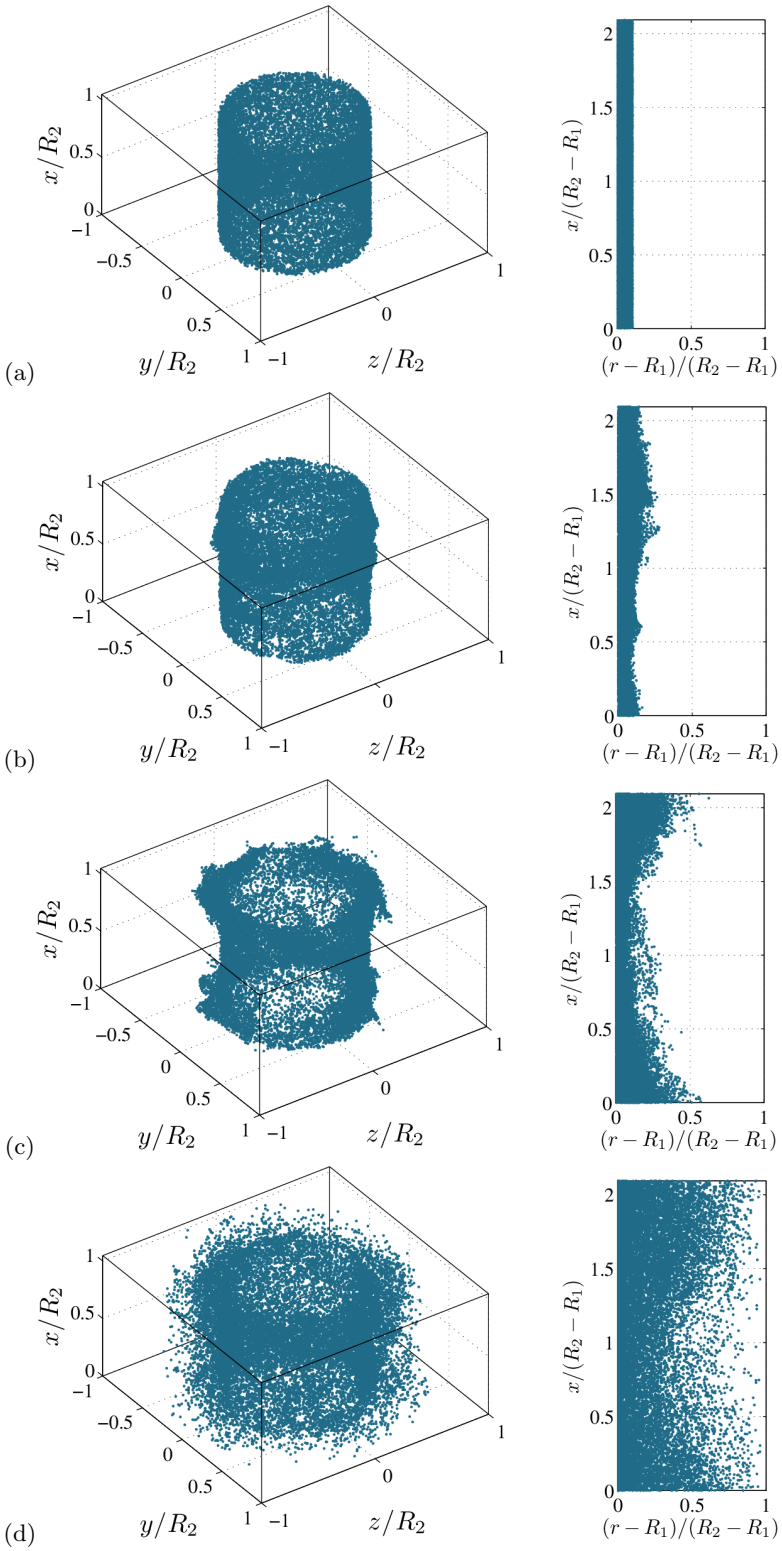

FIG. 19. Bubble positions (3D positions and projection in a $(\mathbf{e_r}, \mathbf{e_x})$ plane) at different times for case 5: (a) Initial positions - (b) after $0.2T_{\Omega 1}$ - (c) after $1.2T_{\Omega 1}$ - (d) after $10.5T_{\Omega 1}$

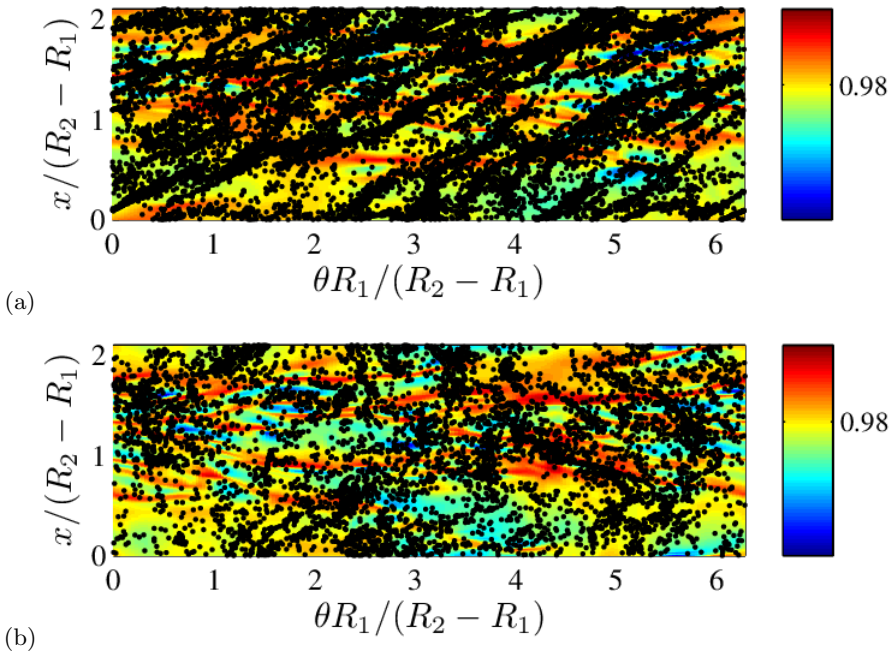

FIG. 20. Bubble positions in the near wall region for $Re = 5000$ at $r_1^+ = 0.19$: (a) case 4 and (b) case 5. The corresponding flow structure without bubble is shown in fig. 17.a

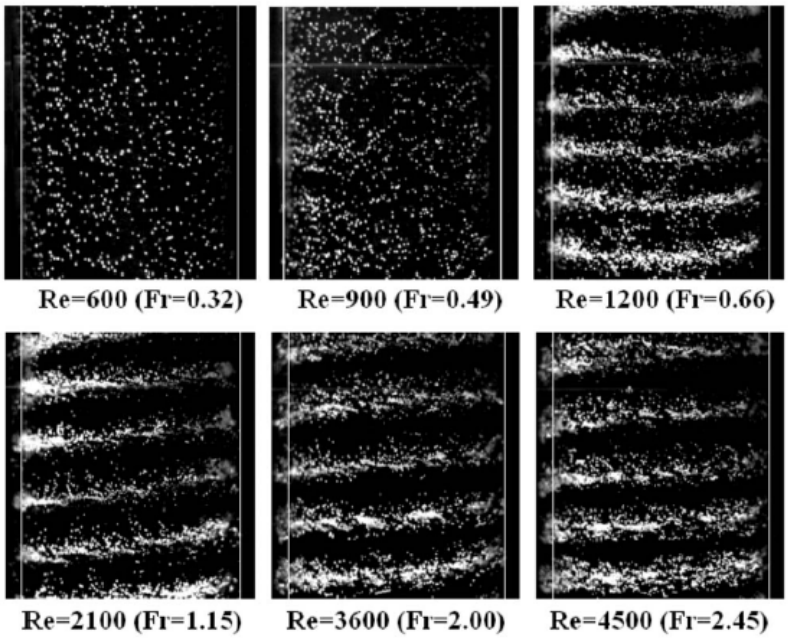

FIG. 21. Side views of spiral bubble arrangement from Murai et al.[19] for $\eta = 0.83$

IV. DISCUSSION

To compare our results with experimental studies, we computed the local void fraction mapped on the Eulerian grid used to simulate the carrying flow. These void fraction profiles are averaged in the axial and azimuthal directions, but not in time. It is thus possible to observe their evolutions in time. In agreement with results discussed above, we observe in fig. 22 that volumetric concentration grows in the near wall region for large bubbles while for the small bubbles the void fraction becomes almost constant throughout the gap. Such bubbles clusters yielding a void fraction peak near the inner cylinder have already been experimentally observed[16,19] for the same range of Reynolds numbers, and also at higher Reynolds numbers[22]. The major difference between our results and the experiments is the location of the accumulation peak, which is very close to the wall in our simulations compared to the experiments. This can be related to the assumption of pointwise bubbles in our simulations. Direct bubble interactions and collisions are neglected in our model which can lead to stronger accumulation than real finite size bubbles experiencing bouncing with neighbors.

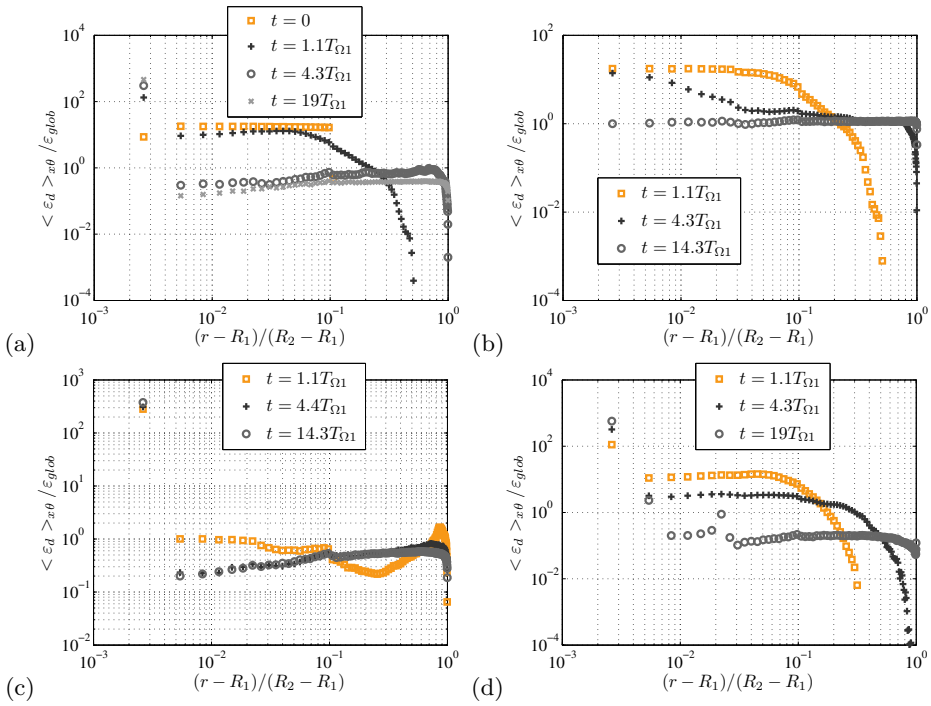

FIG. 22. Average profiles of bubble concentration scaled by the mean void fraction at different times for cases (1 - 2 - 3 - 4) in panels (a - b - c - d), respectively

Those differences in concentration profiles could also be attributed to near-wall hydrodynamic effect. In order to discuss the radial migration, we consider the force balance in the radial direction:

$$(\rho_b + C_M \rho_f)\, \mathcal{V}_b \left(\ddot{r} - \frac{v_\theta^2}{r} \right) = (1 + C_M) \rho_f \mathcal{V}_b \frac{Du_r}{Dt} + F_{L,r} + F_{D,r} \tag{15}$$

For the comparison of the different contributions, we have selected case 1 corresponding to $Re = 5000$ and $g = 0$. Each contribution of the force balance (eq. 15) is averaged on the Eulerian mesh grid. These Eulerian force fields are obtained by averaging over time, azimuthal and axial directions the forces acting on bubbles at a considered radial location. The different contributions are shown in fig. 23. We clearly obtain a negative net balance which explains the strong attraction of bubbles towards the inner cylinder. Force balance

is dominated by inertia (including added-mass) effects. This is driven by the azimuthal rotation of the fluid corresponding to the contribution $-\frac{u_\theta^2}{r}\mathcal{V}_b\rho_f$ of the radial acceleration of the fluid $\frac{Du_r}{Dt} = \frac{\partial u_r}{\partial t} + u_r\frac{\partial u_r}{\partial r} + u_\theta\frac{\partial u_r}{r\partial\theta} + u_x\frac{\partial u_r}{\partial x} - \frac{u_\theta^2}{r}$ as shown in fig. 24. The averaged value is compared to instantaneous and local values of twenty selected bubbles. This force is the major contribution leading to the peak of bubble concentration near the inner cylinder. Realistic void fraction profiles seem then difficult to be numerically reproduced since this force always drives the bubbles towards the inner wall. Sugiyama et al.[24] have also observed those drawbacks of bubble pointwise assumption. They also gave some evidences that the bubble distribution near the wall is very sensitive to the lift force and its modeling.

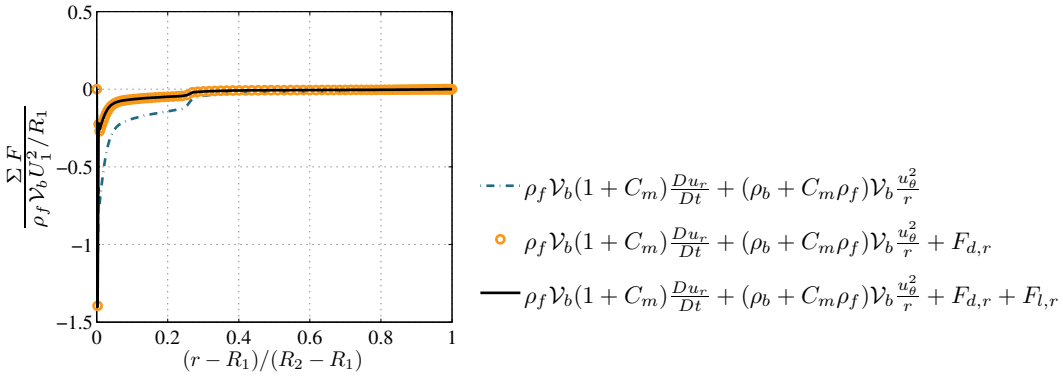

FIG. 23. Sum of radial components of forces experienced by bubbles in case 1 (forces are scaled by $(1+C_m)\mathcal{V}_b\rho_f U_1^2/R_1$)

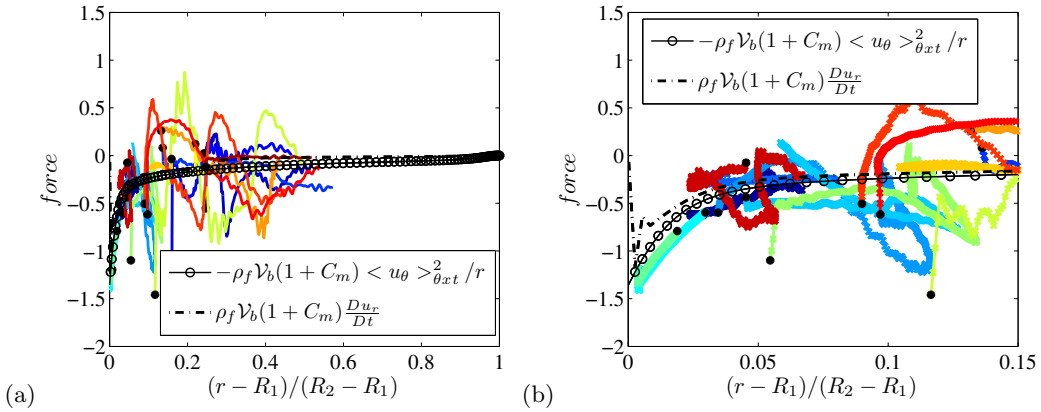

FIG. 24. Relative magnitude of the force balance contributions contained in $\rho_f\mathcal{V}_b(1+C_m)Du/dt$ for case 1. Data are plotted as function of the radial distance to the inner wall for (a) the entire gap and (b) in the vicinity of the inner cylinder. The mean value is compared to $\rho_f\mathcal{V}_b(1+C_m) < U_\theta >^2_{x\theta t}/r$. The instantaneous evolution of this force is also presented for 20 bubbles as a function of their radial positions. All forces have been scaled by $(1+C_m)\mathcal{V}_b\rho_f U_1^2/R_1$

Therefore, we performed additional simulations considering the normal wall correction F_{LW}[51] in the force balance (eq. 9):

$$F_{LW} = C_{LW}\pi R_b^2\rho_f\frac{U_{LW}^2}{2} \tag{16}$$

This force depends on the bubble distance to the wall and on the bubble drift velocity parallel to the wall U_{LW}. The coefficient C_{LW} is positive so that this force induces a

repulsive contribution when the bubble approaches the wall. Those simulations have shown that this correction is not strong enough neither to shift the peak of accumulation away from the inner wall, nor to reduce the accumulation in the herringbone-like streaks. We did not observe inversion ot the motion due to the lift effect in constrast with numerical results of Giusti et al.[52] and Molin et al.[13] in the channel flow configuration. For the range of parameters considered here, the radial motion in the Taylor-Couette flow is controlled by the inertia forces (added mass and pressure gradient) in balance with the drag force.

Considering bubble dispersion in a turbulent Taylor Couette flow, our simulations have shown a weak influence of the Reynolds numbers, but an important sensitivity to the bubble size. Reducing bubble size decreases accumulation in the near-wall region. An estimate of the Stokes numbers indicates that $St \approx 0.1 - 0.2$ for large bubbles (cases 1, 3 and 4) and $St \approx 2.10^{-3}$ for small bubbles (cases 2 and 5). In this latter cases, the time scale of the dispersed phase is very short and small bubbles behave as passive tracers. They respond to small scale energetic fluctuations located around $r^+ \approx 10$. This generates much turbulent dispersion. Additional simulations (not presented here) carried out with small bubbles for $Re = 3000$ and $g = 0$ have revealed similar trends to those observed for $Re = 5000$, i.e. no accumulation in the near-wall herringbone-like streaks and an important turbulent dispersion.

V. CONCLUSION

The first part of our study has consisted in simulating the Taylor-Couette flow in the Turbulent Taylor Vortex Flow regime, with three different geometries. We first validated our simulations by comparing statistics to the literature. After grid convergence tests we chose to focus on geometries with one wavelength λ in the axial direction. Bibliography study highlighted that λ mostly depends on the geometry and on the Reynolds number. Concerning the structure of the flow itself, we observed same trends as described in the literature namely the decomposition of the flow in three mains contributions: a main azimuthal flow driven by the rotation of the inner cylinder, counter-rotative Taylor-Vortices and small scale turbulent fluctuations. The relative amplitude of these three contributions mostly depends on the Reynolds number and the geometry. In the very near wall region, the flow presents similarities with turbulent channel flow such as the linear evolution $u^+ = r^+$ and radial evolution of rms velocities. But the main originality of the flow resides in the presence of the Taylor-Couette vortices inducing Inflow/Outflow regions and the development of streaks with herringbone-shape.

Simulations have been carried out within those regimes to study interaction mechanisms involved in bubble dispersion in Taylor-Couette flows. Bubble dispersion is the consequence of their interaction with these three main contributions of the flow. The rotation of the inner cylinder induces an important attraction towards the inner cylinder through inertia effects. Taylor Vortices have two influences: the outflow jet enhances the global dispersion in the bulk in the radial direction, and circulation of Taylor vortices modifies the migration of bubbles in the axial direction generating accumulation in outflow regions near the inner cylinder. This accumulation is evident for large bubbles ($St \approx 10^{-1}$ and $R_b/\delta^* \approx 1$). Comparison between the influence of these three contributions shows that, for large gap ($\eta = 0.5$), it is the attraction towards the inner cylinder due to its rotation which is here predominant. We modified the force balance in the near wall region to account for particle/wall interaction through repulsive force model, and the force balance in the radial direction kept dominated by inertia induced attraction. Bubbles accumulate in herringbone-like high speed streaks near the inner cylinder. This accumulation along the inner cylinder was expected based on the relative values of the two dimensionless parameters C and H. Compared to bubble accumulation for lower Reynolds number flows (Taylor Vortex Flow or Wavy Vortex Flow), turbulent regime is characterised by the occurence of new flow structures. The small scale turbulent fluctuations has the general tendency to disperse small bubbles characterized by a low Stokes number. No clear accumulation has been observed in these cases.

Gravity effects were also investigated in this study. Larger bubbles migrate towards the inner wall and generate spiral patterns of preferential accumulation. The influence of Taylor vortices is limited by buoyancy effect to the benefit of small scale structures. No accumulation is observed for small bubbles as we can expect considering the results without gravity.

Two main outlooks to this study are related (i) to consider the effect of the bubble deformation on their dispersion and (ii) to describe the flow modulation by the presence of the bubble. Indeed, bubble deformation is known to change the sign of the lift force[53] so that it is expected to impact the bubble accumulation/dispersion. Considering the feedback of the bubbly phase on the continuous one, it can be achieved thanks to two-way coupling simulations. Depending on the scenario of bubble accumulation, important differences on the modification of the flow can lead to torque modulation (increase or reduction of overall drag on the cylinders). Another important issue is to account for direct bubble interactions in the highly accumulated zones of the flow. In those regions, bubble concentration is large and collisions or coalescence are expected to play a significant role on the response of the dispersed phase. Lagrangian tracking needs to be improved beyond the pointwise bubble approximation to restore realistic bubble concentration radial profiles which results as a balance of added-mass centripetal attraction and near-wall shear induced bubble collisions and agitation. Combining (i) and (ii) will then make possible to perform simulation in order to propose a detailed discussion of the experiments showing that bubble deformation is crucial for drag reduction[18,22].

ACKNOWLEDGMENTS

We would like to acknowledge Délégation Générale de l'Armement (DGA) for funding this project. The regional supercomputing centre CALMIP at the University of Toulouse, and the national centres IDRIS and CINES are gratefully acknowledged for their support. We also thank Annaïg Pedrono for her technical support.

[1] A. Davey. The growth of Taylor vortices in flow between rotating cylinders. *J. Fluid Mech.*, 14:336, 1962.
[2] C.D. Andereck, S.S. Liu, and H.L. Swinney. Flow regimes in a circular Couette system with independently rotating cylinders. *J. Fluid Mech.*, 164:155–183, 1986.
[3] J.P. Gollub and H.L. Swinney. Onset of turbulence in a rotating fluid. *Phys. Rev. Lett.*, 35(14), 1975.
[4] D.P. Lathrop, J. Fineberg, and H.L. Swinney. Transition to shear-driven turbulence in Couette-Taylor flow. *Physical Review A*, 46(10), 1992.
[5] S. Dong. Direct numerical simulation of turbulent Taylor-Couette flow. *J. Fluid Mech.*, 587:373–393, 2007.
[6] M. Bilson and K. Bremhorst. Direct numerical simulation of turbulent Taylor-Couette flow. *J. Fluid Mech.*, 579:227–270, 2007.
[7] A. Barcilon, J. Brindley, M. Lessen, and F.R. Mobbs. Marginal instability in Taylor-Couette flows at a very high Taylor number. *J. Fluid Mech.*, 94:453–463, 1979.
[8] S. Dong. Herringbone streaks in Taylor-Couette turbulence. *Phys. Rev. E*, 77(035301(R)), 2008.
[9] G. Sridhar and J. Katz. Effect of entrained bubbles on the structure of vortex rings. *J. Fluid Mech.*, 397:171–202, 1999.
[10] A. Ferrante and S. Elghobashi. On the effects of microbubbles on Taylor-Green vortex flow. *J. Fluid Mech.*, 572:145–177, 2007.
[11] E. Climent and J. Magnaudet. Dynamics of two-dimensional upflowing mixing layer seeded with bubbles: Bubble dispersion and effect of two-way coupling. *Phys. Fluids*, 18(103304), 2006.
[12] I.M. Mazzitelli, D. Lohse, and F. Toschi. The effect of microbubbles on developped turbulence. *Phys. of Fluids*, 15(1), 2003.
[13] D. Molin, C. Marchioli, and A. Soldati. Turbulence modulation and microbubble dynamics in vertical channel flow. *Int. J. Multiphase Flows*, 42:80–95, 2012.
[14] H. Djeridi, J.F. Fave, and Fruman D.H. Bubble capture and migration in Couette-Taylor flow. *Experiments in Fluids*, 26:233–239, 1999.
[15] H. Djeridi, C. Gabillet, and J.Y. Billard. Two-phase Couette-Taylor flow: Arrangement of the dispersed phase and effects on the flow structures. *Physics of Fluids*, 16(1), 2004.
[16] A. Mehel, C. Gabillet, and H. Djeridi. Analysis of the flow pattern modifications in a bubbly Couette-Taylor flow. *Physics of Fluids*, 19(118101), 2007.
[17] T.H. Van den Berg, S. Luther, D.P. Lathrop, and D. Lohse. Drag reduction in Bubbly Taylor-Couette Turbulence. *Phys. Rev. Lett.*, 94(044501), 2005.

[18]T.H. Van den Berg, D.P.M. Van Gils, D.P. Lathrop, and D. Lohse. Bubbly turbulent drag reduction is a boundary layer effect. *Phys. Rev. Lett.*, 98(084501), 2007.
[19]Y. Murai, H. Oiwa, and Y. Takeda. Frictional drag reduction in bubbly Couette-Taylor flow. *Physics of Fluids*, 20(034101), 2008.
[20]Y. Watamura, W. Takeda, and Y. Murai. Intensified and attenuated waves in a microbubble taylor-couette flow. *Physics of Fluids*, 25(054107), 2013.
[21]D.P.M. Van Gils, G.W. Bruggert, D.P. Lathrop, C. Sun, and D. Lohse. The Twente Turbulent Taylor-Couette (T3C) facility : Strongly turbulent (multiphase) flow between two independently rotating cylinders. *Review of scientific intruments*, 82, 2011.
[22]D.P.M. Van Gils, D. Narzeo Guzman, C. Sun, and D. Lohse. The importance of bubble deformability for strong drag reduction in bubbly turbulent taylor-couette flow. *J. Fluid Mech.*, 722:317–347, 2013.
[23]E. Climent, M. Simonnet, and J. Magnaudet. Preferential accumulation of bubbles in Couette-Taylor flow patterns. *Physics of Fluids*, 19(083301), 2007.
[24]K. Sugiyama, E. Calzavarini, and D. Lohse. Microbubbly drag reduction in Taylor-Couette flow in the wavy vortex regime. *J. Fluid Mech*, 608:21–41, 2008.
[25]D. Legendre and J. Magnaudet. The lift force on a spherical bubble in a viscous linear shear flow. *J. Fluid Mech*, 368:81–126, 1998.
[26]I. Calmet and J. Magnaudet. Statistical structure of high-reynolds number turbulence close to the free surface of an open-channel flow. *J. Fluid Mech*, 474:355, 2003.
[27]J.E. Burkhalter and E.L. Koschmieder. Steady supercritical Taylor vortex flow. *J. Fluid Mech.*, 58:547–560, 1973.
[28]J.E. Burkhalter and E.L. Koschmieder. Steady supercritical Taylor vortices after sudden starts. *The Physics of Fluids*, 17(11), 1974.
[29]D. Coles. Transition in circular Couette flow. *J. Fluid Mech.*, 21:385–425, 1965.
[30]A. Racina. *Vermischung in Taylor-Couette Strömung*. PhD thesis, Université de Karlsruhe, juillet 2008.
[31]A. Mehel. *Étude expérimentale d'un écoulement diphasique de Taylor Couette*. PhD thesis, Université de Nantes, Juin 2006.
[32]A. Bouabdallah. *Instabilités et turbulence dans l'écoulement de Taylor-Couette*. PhD thesis, Institut National Polytechnique de Lorraine, juin 1980.
[33]E.L. Koschmieder. Turbulent Taylor Vortex Flow. *J. Fluid Mech.*, 93:515–527, 1979.
[34]A. Barcilon and J. Brindley. Organized structures in turbulent Taylor-Couette flow. *J. Fluid Mech.*, 143:429–449, 1984.
[35]F. Wendt. Turbulente Strömungen zwischen zwei rotierenden konaxialen Zylindern. *Ingenieur Archiv*, 1933.
[36]R. Ostilla Monico, S.G. Huisman, T.J.G. Jannink, D.P.M Van Gils, R. Verzicco, S. Grossmann, C. Sun, and D. Lohse. Optimal Taylor-Couette flow: radius ratio dependence. *Arxiv*, (1304.6331v2), 2013.
[37]S. Merbold, H.J. Brauckmann, and C. Egbers. Torque measurements and numerical determination in differentially rotating wide gap Taylor-Couette flow. *Phys. Rev. E.*, 87(023014), 2013.
[38]J. Kim, P. Moin, and R. Moser. Turbulence statistics in fully developed channel flow at low reynolds number. *J. Fluid Mech.*, 177:133–166, 1987.
[39]B. Eckhardt, L. Grossmann, and D. Lohse. Torque scaling in turbulent Taylor-Couette flow between independently rotating cylinders. *J. Fluid Mech.*, 581:221–250, 2007.
[40]D. Pirrò and M. Quadrio. Direct numerical simulation of turbulent Taylor-Couette flow. *European Journal of Mechanics B/Fluids*, pages 552–566, 2008.
[41]G.P. Smith and A.A. Townsend. Turbulent Couette flow between concentric cylinders at large Taylor numbers. *J. Fluid Mech.*, 123:187–217, 1982.
[42]S.G. Huisman, S. Scharnowski, C. Cierpka, J. Kähler, D. Lohse, and C. Sun. Logarithmic boundary layers in strong Taylor-Couette turbulence. *Phys. Rev. Let.*, 110(264501), 2013.
[43]S. Grossmann, C. Sun, and D. Lohse. Velocity profiles in strongly turbulent Taylor-Couette flow. *Arxiv*, (1310.6196v1), 2013.
[44]J. Magnaudet and I. Eames. The motion of high-reynolds number bubbles in inhomogeneous flow. *Ann. Rev. Fluid Mech.*, 32:659–700, 2000.
[45]R. Mei, J.F. Klausner, and Lawrence C.J. A note on the history force on a spherical bubble at finite Reynolds number. *Phys. Fluids*, 6(1):418–420, 1994.
[46]A. Merle, D. Legendre, and J. Magnaudet. Forces on a high-re spherical bubble in a turbulent flow. *J. Fluid Mech.*, 532:53–62, 2005.
[47]E. Climent and J. Magnaudet. Large-Scale Simulations of Bubble-Induced Convection in a Liquid Layer. *Physical Review Letters*, 82(24), 1999.
[48]D. Legendre, C. Colin, J. Fabre, and J. Magnaudet. Influence of gravity upon the bubble distribution in a turbulent pipe flow: comparison between numerical simulations and experimental datas. *Journal de Chimie Physique*, 96(6):951–957, 1999.
[49]T. Wei, E.M. Kline, S.H.-K. Lee, and S. Woodruff. Görtler vortex formation at the inner cylinder in Taylor-Couette flow. *J. Fluid Mech.*, 245:47–68, 1992.
[50]Brauckmann H.J. and Eckhardt B. Direct numerical simulations of local and global torque in taylor-couette flow up to re=30000. *J. Fluid Mech.*, 718:398, 2013.
[51]F. Takemura and J. Magnaudet. The transverse force on clean and contamined bubbles rising near a vertical wall at moderate Reynolds number. *J. Fluid Mech*, 495:235–253, 2003.

[52]A. Giusti, F. Lucci, and A. Soldati. Influence of the lift force in direct numerical simulation of upward/downward turbulent channel flow laden with surfactant contaminated microbubbles. *Chemical Engineering Science*, 60:6176–6187, 2005.

[53]R. Adoua, D. Legendre, and J. Magnaudet. Reversal of the lift force on an oblate bubble in a weakly viscous linear shear flow. *J. Fluid Mech.*, 628:23–41, 2009.